



UPPSALA
UNIVERSITET

*Digital Comprehensive Summaries of Uppsala Dissertations
from the Faculty of Science and Technology 909*

Thermal Radiation from Co-evaporated $\text{Cu}(\text{In}, \text{Ga})\text{Se}_2$

End point detection and process control

JENS SCHÖLDSTRÖM



ACTA
UNIVERSITATIS
UPSALIENSIS
UPPSALA
2012

ISSN 1651-6214
ISBN 978-91-554-8306-7
urn:nbn:se:uu:diva-170437

Dissertation presented at Uppsala University to be publicly examined in Polhemssalen, Ångströmlaboratoriet, Lägerhyddsvägen 1, Uppsala. Thursday, April 26, 2012 at 09:30 for the degree of Doctor of Philosophy. The examination will be conducted in English.

Abstract

Schöldström, J. 2012. Thermal Radiation from Co-evaporated Cu(In,Ga)Se₂: End point detection and process control. Acta Universitatis Upsaliensis. *Digital Comprehensive Summaries of Uppsala Dissertations from the Faculty of Science and Technology* 909. 66 pp. Uppsala. ISBN 978-91-554-8306-7.

The use of solar cells for energy production has indeed a bright future. Reduction of cost for fabrication along with increased efficiency are key features for a market boom, both achieved as a result of increased knowledge of the technology. Especially the thin film solar cell technology with absorbers made of Cu(In,Ga)Se₂ (CIGS) is promising since it has proven high power conversion efficiency in combination with a true potential for low cost fabrication.

In this thesis different recipes for fabrication of the Cu(In,Ga)Se₂ absorber layer have been studied. The deposition technique used has been co-evaporation from elemental sources. For all depositions the substrate has been heated to a constant temperature of 500 °C in order for the growing absorber to form a chalcopyrite phase, necessary for the photovoltaic functionality. The selenium has been evaporated such to always be in excess during depositions whereas the metal ratio Cu/(In+Ga) has been varied according to different recipes but always to be less than one at the end of the process. In the work emphasis has been on the radiative properties of the CIGS film during growth.

The substrate heater has been temperature controlled to maintain the constant set temperature of the substrate, regardless of varying emitted power caused by changing surface emissivity. Depending on the growth conditions the emissivity of the growing film is changing, leading to a readable variation in the electrical power to the substrate heater.

Since the thermal radiation from the substrate during growth has been of central focus, this has been studied in detail. For this reason the substrate has been treated as an optical stack composed of glass/Mo/Cu(In,Ga)Se₂/Cu_xSe which determine the thermally radiated power by its emissivity. An optical model has been adopted to simulate the emissivity of the stack. In order to use the model, the optical constants for Cu(In,Ga)Se₂ and Cu_xSe have been derived for the wavelength interval 2 μm to 20 μm. The simulation of the emissivity of the stack during CIGS growth agreed well with what has been seen for actual growth. Features of the OP-signal could hereby be explained as a result of film thickness of Cu(In,Ga)Se₂ and Cu_xSe respectively. This is an important knowledge for an efficient fabrication in large scale.

Keywords: CIGS, Cu(InGa)Se₂, thin film, solar cells, end point detection, process control, optical constants, Cu_xSe

Jens Schöldström, Uppsala University, Department of Engineering Sciences, Solid State Electronics, Box 534, SE-751 21 Uppsala, Sweden.

© Jens Schöldström 2012

ISSN 1651-6214

ISBN 978-91-554-8306-7

urn:nbn:se:uu:diva-170437 (<http://urn.kb.se/resolve?urn=urn:nbn:se:uu:diva-170437>)

*With love to my four girls An-
neli, Astrid, Vendela and Idun
for their encouragement and
their incredible patience...*

List of papers

- I J. Kessler, J. Schöldström and L. Stolt, "RAPID Cu(In,Ga)Se₂ GROWTH USING "END POINT DETECTION"", in: Proceedings 28th IEEE Photovoltaic Specialist Conference, Anchorage (2000) p. 509-512
- II J. Kessler, J. Schöldström, and L. Stolt, "ANALYSIS OF CIGS FILMS AND DEVICES RESULTING FROM DIFFERENT Cu-RICH TO Cu-POOR TRANSITIONS", in Proceedings 17th European Photovoltaic Energy Conference, Munich, 2001, p. 1019.
- III M. Bodegård, J. Kessler, O. Lundberg, J. Schöldström and L. Stolt, "Growth of Co-evaporated Cu(In,Ga)Se₂ – The Influence of Rate Profiles on Film Morphology", in: Proceedings Materials Research Society (2001) p. 2.2.1
- IV J. Kessler, C. Chityuttakan, J. Schöldström, and L. Stolt, "GROWTH OF Cu(In,Ga)Se₂ FILMS USING A Cu-POOR/RICH/POOR SEQUENCE: SUBSTRATE TEMPERATURE EFFECTS", Thin Solid Films 431-432 (2003) 1-5
- V J. Kessler, C. Chityuttakan, J. Lu, J. Schöldström and L. Stolt, "Cu(In,Ga)Se₂ Thin Films Grown with a Cu-Poor/Rich/Poor Sequence: Growth Model and Structural Considerations", Progress In Photovoltaics: Research and Applications 2003; 11:319–331 (DOI: 10.1002/pip.495)
- VI U. Zimmermann, J. Schöldström, M. Edoff, and L. Stolt, "Thermodynamic simulation of the endpoint characteristics in a CIGS deposition process", in: proceedings of the 19th EUPVSEC, Paris : Contribution 4AV.1.68 (2004)
- VII J. Schöldström, J. Kessler, M. Edoff, "Two-stage growth of smooth Cu(In,Ga)Se₂ films using end-point detection", Thin Solid Films 480–481 (2005) 61– 66
- VIII J. Schöldström, U. Zimmermann, M. Bodegård, "Determination of the optical constants for Cu(In,Ga)Se₂ and Cu_xSe in the IR region", Journal of Physics D: Applied Physics 45 (2012), p. 1-10, DOI:10.1088/0022-3727/45/11/115101
- IX J. Schöldström, U. Zimmermann, M. Bodegård, "Dynamic radiative properties of the Cu(In,Ga)Se₂ layer during the coevaporation process", Progress In Photovoltaics: Research and Applications 2010; 18:321–327 DOI: 10.1002/pip.931

The contribution by the author to the included publications in this thesis is as follows:

- I Most of the planning of the experimental work. All experimental work. Most of the evaluation.
- II Most of the planning of the experimental work. All experimental work. Most of the evaluation, and part of the writing.
- III Part of the experimental work. Part of the evaluation.
- IV Part of the development of the experimental methods. Part of the evaluation.
- V Part of the development of the experimental methods. Part of the evaluation.
- VI Original idea for the paper. Suggestion of input parameters. Part of the evaluation.
- VII All planning, all experimental work, most of the evaluation and all writing.
- VIII All planning, all experimental work, most of the evaluation and all writing.
- IX All planning, all experimental work, most of the evaluation and all writing.

Contents

1. Introduction	9
1.1 The use of solar cells for power generation	9
1.2 The photovoltaic function of the solar cell	11
1.3 Solar cell quality measurements	12
1.3.1 I-V Measurements	13
1.3.2 QE Measurements	14
2. The CIGS material	16
2.1 The choice of Cu(In,Ga)Se ₂ as absorber	17
2.2 The structure of the CIGS solar cell	18
3. The growth of the Cu(In,Ga)Se ₂ absorber layer	20
3.1 Equipment	20
3.2 The co-evaporation	24
3.3 Segregated phase of Cu _x Se	25
3.4 Radiative properties of CIGS during growth	26
3.5 The use of End-Point-Detection	28
3.6 The two-stage CURO deposition process	29
3.7 The three-stage process CUPRO	34
3.8 The INRO process	36
3.9 The constant power mode	37
4. Simulation of the growth process	42
4.1 The optical model	42
4.2 Determination of the optical constants for CIGS and Cu _x Se	43
4.3 Results from the simulations	49
5. Conclusion and outlook	54
7. Summary in Swedish	56
7.1 Solenergi	56
7.2 Solcellen	56
7.3 CIGS-solceller	57
7.4 Sammansättningskontroll och CIGS-processer	58
7.5 IR-emissivitet hos CIGS-skikt	60

1. Introduction

1.1 The use of solar cells for power generation

Today's massive exploitation of fossil fuels imposes a major threat to the environment in terms of emission of greenhouse gases and acid rain. Around 80% of all energy used worldwide originates from fossil fuels like coal, oil and natural gas [1], and the global energy demand is projected to grow by 1.6% per year on average or 45% in total from 2006 to 2030. Oil remains the dominant fuel though demand for coal rises strongly, mainly driven by the economic growth in China and India. The share of nuclear power in primary energy demand is expected to decrease from 6% today to 5% in 2030.

At the same time, the use of modern renewable energy technologies grows rapidly. Falling costs as renewable technologies mature, assumed higher fossil-fuel prices and strong policy support provide an opportunity for the renewable industry to eliminate its reliance on subsidies and to bring emerging technologies into the mainstream. Wind, solar, geothermal, tide and wave energy together grow faster than any other source worldwide, at an average rate of 7.2% per year over the coming 20 years [1].

One of the most promising solar energy technologies for power generation is photovoltaics (PV). Photovoltaic devices, or solar cells, use semiconductor materials to convert sunlight directly into electricity. Power is produced when sunlight strikes the semiconductor material and creates electric voltage and current. After its invention and commercial development starting in the 1950's, solar cells were used primarily in space applications and consumer type applications. However, as the production technologies have improved over the past two decades and resulted in less costly and better performing solar cells, there has been a growing interest to use PV for large-scale power generation. Today, photovoltaics is a fully recognized source of renewable energy with the potential to give a substantial input to the global energy supply in the future, and to be part of creating a sustainable energy system.

The last decade has seen a robust and continuous growth in installed PV capacity, see Figure 1, and it is expected to continue in the coming years. Currently, the world's cumulative PV power installed is almost 40 GW which produce about 45 TWh of electricity on a yearly basis [2].

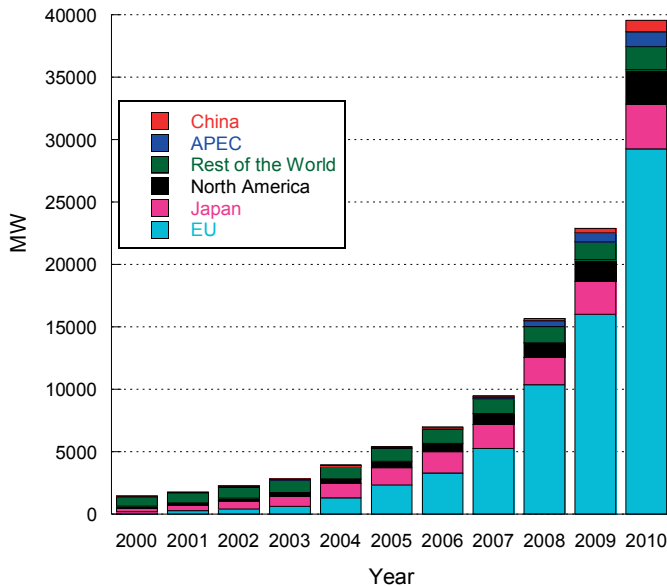


Figure 1: Historical development of world cumulative PV power installed in main geographies. Data from European Photovoltaic Industry Association [2].

A key driver to the impressive increase of PV installations and the resulting explosive growth in the photovoltaic industry has been government incentives. The PV industry is chasing a trillion Euro energy market, but it is also economically unviable today. Without subsidies, PV energy would not today be able to compete with conventional energy sources. Lowering the production costs of PV modules and system components is crucial if the vision of solar power as a core energy generation technology is ever to be achieved.

Solar cells and modules can be divided into two main categories: wafer-type and thin-film. Wafer-type cells are made from silicon wafers cut from a rod or an ingot, or from silicon ribbons. Thin film cells are deposited directly onto a substrate, usually glass, stainless steel, or plastic. The wafer-based silicon technology has proven excellent stability and reliability, with modules operating under outdoor conditions over several decades, showing none or only minor deterioration in performance. Its only drawback has been the relatively costly production, mainly due to the expensive raw materials and low material yield during the fabrication process. Therefore, much of the research efforts within photovoltaics over the past three decades have been devoted to finding new materials and fabrication processes with a higher potential of cost reduction than that of the crystalline silicon technology. The key factors to reducing the production costs of PV modules are to increase their conversion efficiency and reduce their materials use. Thin-film solar cells need much less active material than wafer-type solar cells to generate electricity. Their weak point have been low conversion efficiencies, but in recent

years several promising technologies for thin-film solar cells have shown to be very efficient in converting the power of the sun light into electric power [3].

1.2 The photovoltaic function of the solar cell

The essential part in a solar cell, see Figure 2, is the pn-junction. It consists of two semiconductor layers, one n-doped layer with an excess of free electrons which originate from dopant atoms which can easily free one electron, and one p-doped layer where holes i.e. absence of electrons are in excess. The holes originate from ionized dopant atoms which can easily accept one extra electron. In an n-type material electrons act as mobile charge carriers, whereas holes act as charge carriers in the p-type material. When a junction is formed between two layers of different type of doping, diffusion makes electrons travel from the n-type side to the p-type side, while ionized dopant atoms are left. As a consequence, a region depleted of free charge carriers is created and an electric field is built up by the ionized dopant atoms on the p- and n-doped sides respectively. Thereby an electrostatic potential is formed between the quasi neutral parts of the n-type and the p-type semiconductors. The electric field is the engine in the photovoltaic cell and will separate positive and negative free charge i.e. electron hole pairs created by the absorption of light. Absorption will occur for photon energies above the band gap of the semiconductors and the amount of absorbed photons and thereby created electron hole pairs will depend on the thickness of the semiconductor and its absorption coefficient. If an electron-hole-pair is created in, or within a diffusion length from the depletion region, the electron (on the p-type side) or the hole (on the n-type side) will drift in the electric field, and travel to the opposite side. In steady state condition, when light is shining onto the solar cell, many electron-hole-pairs are generated and also separated by the electric field causing a build-up of negative charge on the n-side and positive charge on the p-side. To make use of the pn-diode as a power generating solar cell, a load may be connected between the n-side and the p-side and current will flow through the load. In order to collect the current in an efficient way, both sides of the pn-diode must have contact layers with good ohmic contacts to the semiconductor materials. For the back side, which does not need to be optically transparent, this is made by a layer of metal, the back-contact. The contact on the front side must be both electrically conducting and optically transparent, and is commonly called a window layer.

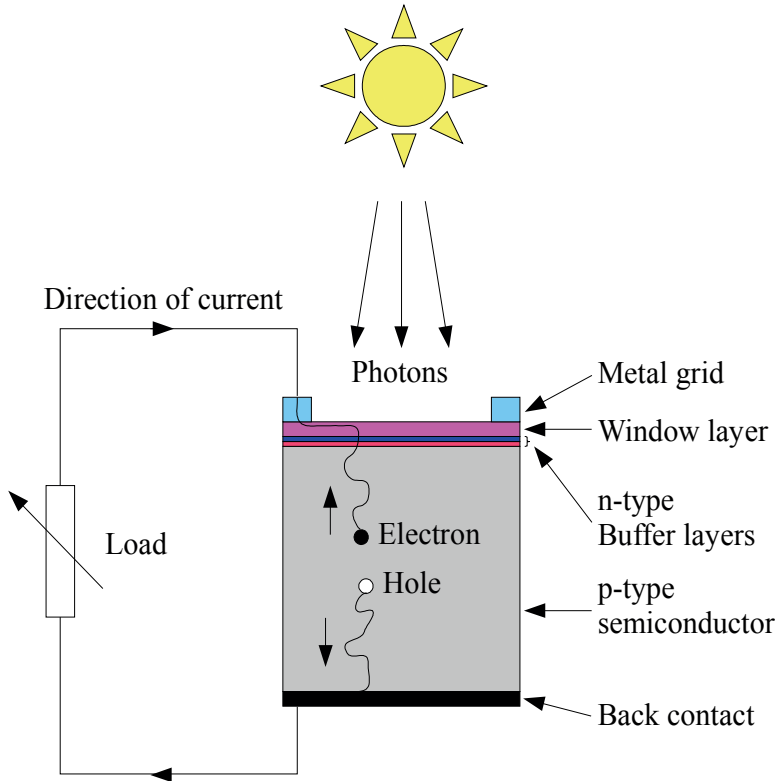


Figure 2: A very simplified picture of solar cell device at work. Photons (quanta of light) from the sun travels through the window layer of the solar cell and further down into the absorber. Somewhere in the absorber the photon may excite an electron-hole pair. The electron and the hole will be separated by the internal electric field in the pn-junction. Due to the separation of the different charges, a voltage is built up. The more photons that are being absorbed, the more electric current will the solar cell produce when connected to a load.

1.3 Solar cell quality measurements

To produce high quality solar cells both in the laboratory scale and in the industrial scale, a reliable feed back loop is necessary. Different quality measurements of the solar cell may indicate deviations from what could be expected such as poor ohmic contacts between back contact and absorber layer, or excessively high light absorption in the window layer. Two of the most important measurements to be performed on the solar cells are I-V measurement and QE measurement.

1.3.1 I-V Measurements

The most common test of the electric properties of the solar cell is by measuring the relationship between the current passing through the cell and the voltage across the cell under illumination, see Figure 3. The voltage across the cell when no current flows is called the open circuit voltage and is denoted V_{OC} . The current flowing through the device at short circuit conditions is called short circuit current and is denoted I_{SC} . Since the essential part of the solar cell consists of a pn-diode, the characteristic relation between voltage and current are following the diode equation shown in Equation 1. In the diode equation, I_0 is the saturation current for the diode, $q = 1.602 \times 10^{19} \text{ C}$ is the elementary charge, n is an ideality factor for the diode, $k_B = 1.381 \times 10^{-23} \text{ JK}^{-1}$ is the Boltzmann constant, T is the temperature in Kelvin for the diode and I_L is the photo-generated current.

$$I = I_0 (e^{q \cdot V / (n \cdot k_B \cdot T)} - 1) - I_L \quad (1)$$

The point at the diode curve where the maximum power occurs (the maximum power point) is described by the voltage and current at maximum power point, V_{MP} and I_{MP} . The electrical conversion efficiency for the solar cell is denoted η and is the ratio between the maximum power and the power of the irradiated light. It is described by Equation 2. Another way of describing the quality of the solar cell is by using the fill factor, which is the ratio between the max power and the product of V_{OC} and I_{SC} . A high fill factor is indicative of good diode properties and usually is connected to high efficiency. The fill factor is defined in Equation 3.

$$\eta \equiv \frac{V_{MP} \cdot I_{MP}}{P_{Light}} \quad (2)$$

In Equation 2, P_{Light} is the total power of the light onto the solar cell.

$$FF \equiv \frac{V_{MP} \cdot I_{MP}}{V_{OC} \cdot I_{SC}} \quad (3)$$

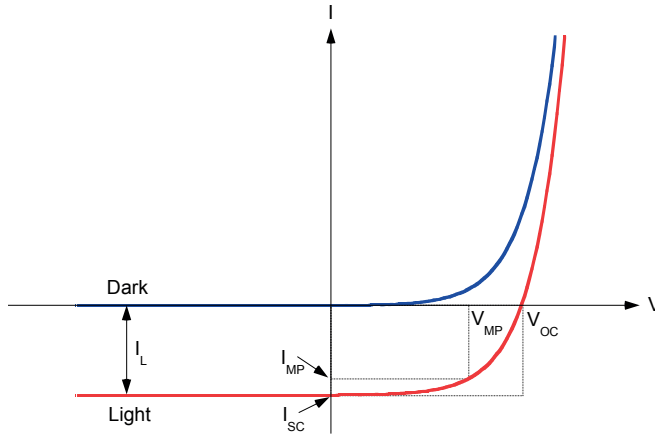


Figure 3: Current-voltage characteristic for a solar cell measured in dark and light conditions. The most important solar cell parameters are indicated in the graph.

1.3.2 QE Measurements

As can be seen in Figure 4, the light emitted by the sun that reaches the surface of the earth, has wavelengths from $0.3 \mu\text{m}$ up to $2.5 \mu\text{m}$.

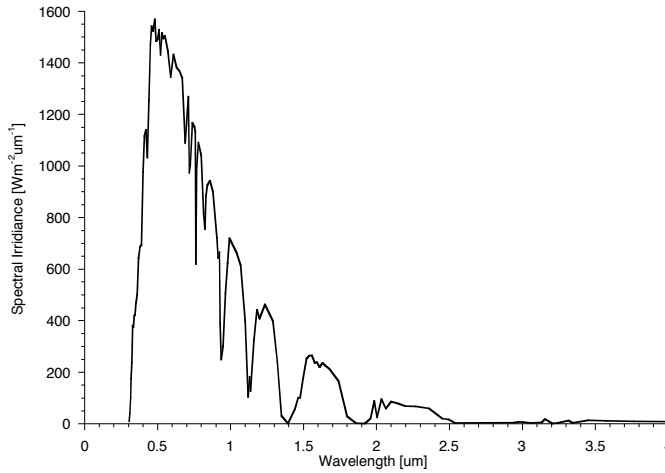


Figure 4: Reference solar spectral irradiance distribution AM1.5 from IEC-904-3[4].

In order to investigate the wavelength dependent current generation a quantum efficiency ($QE(\lambda)$) measurement, is performed. In a QE measurement, filtered light in narrow wavelength intervals is used to illuminate the cell. For each interval the short circuit current is measured. Since the short circuit current for each cell equals the light generated current I_L , the ratio of

the light generated current to the intensity of the incoming light for each interval can be calculated. If every in-coming photon in a certain wavelength interval would generate one collected electron, the QE response for this wavelength would be one. If no current is generated, the QE response is zero. The QE measurement gives information about the band gaps of the materials in a solar cell. A graph of a typical QE measurement can be seen in Figure 5. As can be seen for photons with wavelengths corresponding to energy less than the optical band gaps, the QE response is zero. Absorption of photons in window layers above the absorber may decrease the QE response. Other loss mechanisms can be reflection at the surface of the solar cell and poor absorption in the absorber. A poor collection of generated charge carriers would also decrease the QE. This can be due to high recombination in the cell.

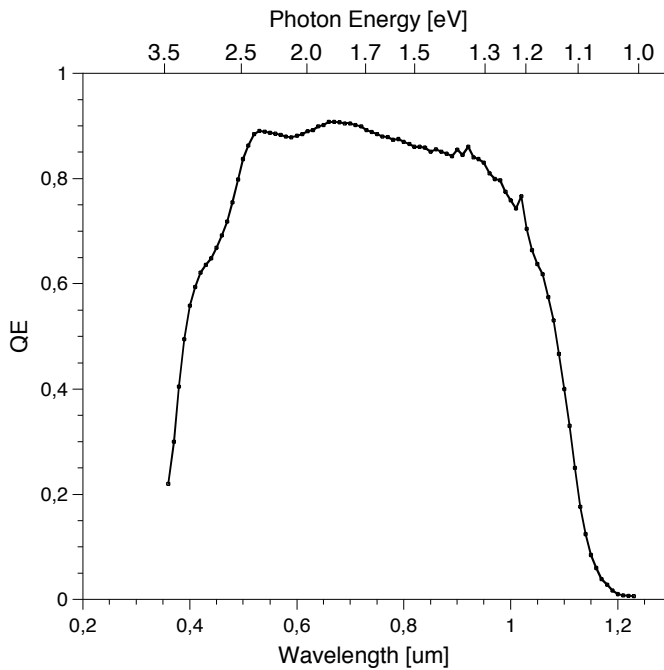


Figure 5: A quantum-efficiency diagram, QE, from a solar cell showing the ratio between collected electrons and incoming photons as a function of wavelength. Ideally the QE response should be one for the entire wavelength range below the wavelengths corresponding to the band gap, which would mean that every incoming photon managed to generate one electron-hole pair.

2. The CIGS material

$\text{Cu}(\text{In,Ga})\text{Se}_2$, CIGS, is an alloy of the two ternary compounds CuInSe_2 , CIS, and CuGaSe_2 , CGS. This alloy can be varied continuously between CIS and CGS. The indium and gallium atoms will occupy the group III sites in the CIGS lattice in a random way. Hence, a common designation is $\text{Cu}(\text{In}_{1-x},\text{Ga}_x)\text{Se}_2$, for x between 0 and 1, or expressed as in Equation 4.

$$x = [\text{Ga}] / ([\text{In}] + [\text{Ga}]) \quad (4)$$

The crystal lattice forms a chalcopyrite structure seen in Figure 6. When thin films of CIGS are grown by co-evaporation the films become poly-crystalline with grain sizes of about one micrometer, and with the crystal orientation, random or with a preferred orientation. In Figure 7, a scanning electron image of a cross section CIGS solar cell is shown. The size of the CIGS grains is between 0.3–1 μm .

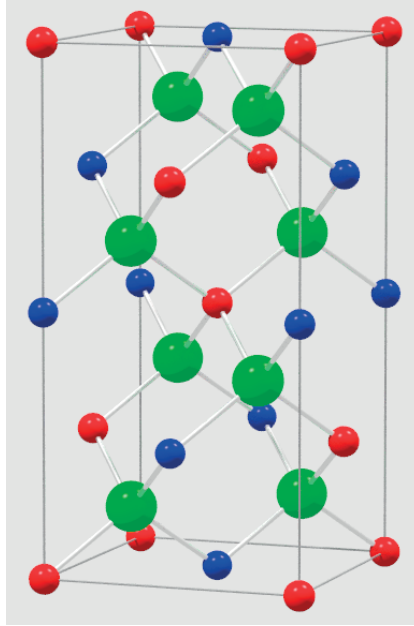


Figure 6: The unit cell of chalcopyrite phase $\text{Cu}(\text{In,Ga})\text{Se}_2$. Green spheres: selenium, blue: Indium or Gallium, red: copper.

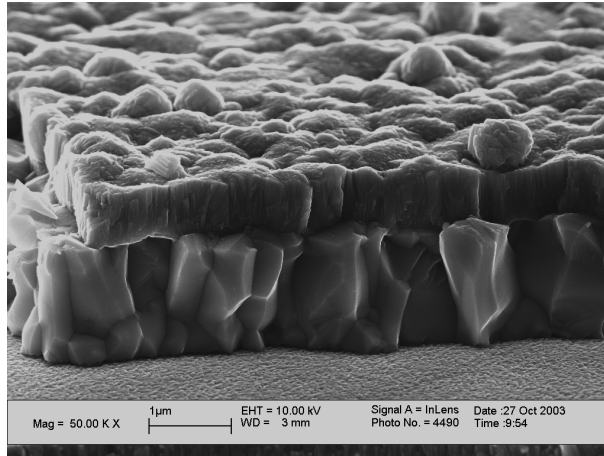


Figure 7: A scanning electron microscope, SEM, image of a CIGS solar cell. In cross section the CIGS layer with ZnO on top can be seen. The structure is deposited on a surface of sputtered Mo (bottom part of image). There is also a thin CdS film between the CIGS and ZnO layers, but the magnification is not sufficient to resolve this film.

2.1 The choice of Cu(In,Ga)Se_2 as absorber

In order to be as efficient as possible the absorber shall absorb virtually all incoming photons with energies above the band gap energy of CIGS. Since the absorption of light in matter is proportional to an exponential expression, $\exp(-\alpha x)$ where α is a coefficient of absorption, and x is the depth in the material, the absorber must be sufficiently thick. The semiconductor material Cu(In,Ga)Se_2 has a direct band gap, which means that a photon with energy above the band gap energy has a very high probability to generate an electron-hole pair even for very thin layers. Thus, the absorption coefficient is very high. This is not the case for all semiconductors. Crystalline silicon for example, has an indirect band gap and is dependent of phonons together with suitable photons to create electron-hole pairs. For this reason, the probability of a photon to be absorbed is much less in a semiconductor with indirect band gap than one with direct, and hence, the necessary thickness required for full absorption in silicon will be about two orders of magnitude larger than that required for CIGS. Solar cells with absorbers made of Cu(In,Ga)Se_2 have been fabricated since decades [5] and proved to be very suitable for high efficiency solar cells. When fabricating the Cu(In,Ga)Se_2 material for solar cells, defects in the crystal lattice are created automatically. Some of these defects act as dopants for the semiconductor, and the material is said to be auto-doped. Some defects will be passivated by the formation of charge neutral clusters [6]. Since the formation energy of the neutral clusters

is very low, the material can accommodate a large number of defects. This feature makes the Cu(In,Ga)Se_2 less sensitive for proton and electron radiation, and hence very suitable also for space applications [7, 8].

Two other very important criteria for the performance of a solar cell is believed to be the lattice matching and the band gap matching with the n-type partners in the solar cell, the buffer layer and the transparent front contact layer. The ability to choose the gallium content, x , gives a span in achieved band gap from 1.04 eV for $x = 0$ (pure CIS) up to 1.68 eV for $x = 1$ (pure CGS) [9]. Today, CIGS with $\text{Ga}/(\text{Ga}+\text{In})$ values below 0.5 in combination with CdS buffer layers deposited by chemical bath deposition are most commonly used. It seems that the corresponding CdS/CIGS band line-up works well.

2.2 The structure of the CIGS solar cell

This thesis is mainly focused on the CIGS absorber. All other necessary layers to constitute a complete solar cell, are performed according to the state-of-the-art solar cell line at the Ångström Solar Center [10], described briefly below. A picture of the complete structure is shown in Figure 8.

The substrate is standard soda-lime glass commonly used for windows. It is a low cost material, easily available in large quantities. This glass contains sodium, which has been shown to have positive influence on the growth of Cu(In,Ga)Se_2 grains [11] and also on the electrical properties of the CIGS layer [12]. In the scope of this thesis the substrate thickness used for experiments is mostly one millimeter, and the lateral size usually 100 mm by 100 mm. After a soap and water cleaning in an ultrasonic bath, the substrates are coated with molybdenum by DC magnetron sputtering which will constitute the back contact. The thickness of the molybdenum layer is about 400 nanometers, which gives satisfying electrical sheet resistivity. The molybdenum sputter process is tuned to allow sodium to diffuse from the substrate into the growing Cu(In,Ga)Se_2 during the co-evaporation of the absorber. Preferably, the back contact should also serve as reflector for photons that have crossed the absorber without being absorbed. This increases the probability to generate electron-hole-pairs, and still use very thin CIGS absorbers. The molybdenum back contact is not optimal for this purpose, so experiments have been performed to deposit another film between the molybdenum back contact and the CIGS absorber, in order to increase the reflectance [13,14]. After deposition of the back contact, the co-evaporation of the CIGS absorber is performed. This will be described in detail later on.

Since Cu(In,Ga)Se_2 layer is p-type, the other layers to constitute a pn-diode must have n-type conduction properties. The n-type partners are chosen to have good matching to the CIGS layer as described in section 2.1. The first layer is called the buffer layer and in most cases consists of a thin (50

nm) CdS layer deposited with a wet chemical process (CBD). Two layers of ZnO are subsequently deposited by rf (radio frequency) or pulsed DC magnetron sputtering, one non-doped highly resistive layer and one doped with aluminium. The role of the first highly resistive layer is to provide protection against possible shunting paths and the second to provide a top contact with high conductivity. This type of pn-junction made up with different materials is called a heterojunction, in contrast to a homojunction where the same semiconductor is used, but doped differently. The position in the Cu(In,Ga)Se₂/CdS/i-ZnO structure where the conduction type changes from p-type to n-type is debated [16]. An n-type ordered vacancy compound, OVC, surface layer is suggested to be formed from Cu(In,Ga)Se₂ by electromigration of copper atoms from the surface to the bulk. X-ray Photoelectron Spectroscopy, XPS, measurements have revealed a composition close to Cu₁(In,Ga)₃Se₅ [15]. If this is correct, the point of the junction will be entirely within the CIGS layer and not at the interface between the CIGS and the buffer. Since all interfaces normally are points of high recombination, moving the junction into the CIGS layer, may partly explain the high junction quality of the CIGS/CdS solar cell, which then more resembles a homojunction than a true heterojunction. Recent research has shown promising results to substitute the CdS buffer with a more environmentally friendly buffer of Zn_{1-x}Mg_xO or Zn(O,S) [17].

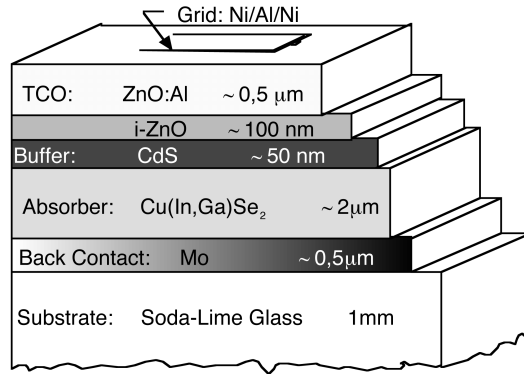


Figure 8: Schematic view of the layers involved to build up the complete solar cell. Worth to mention is that promising research is going on to exchange the CdS layer. Not shown in the picture is a top coating referred to as anti-reflective, AR, layer sometimes used to maximize the electrical conversion efficiency.

3. The growth of the $\text{Cu}(\text{In,Ga})\text{Se}_2$ absorber layer

3.1 Equipment

The equipment that has been used for co-evaporation of the $\text{Cu}(\text{In,Ga})\text{Se}_2$ absorber is a modified Balzer UMS 500 p-system, which is shown in Figure 9. The central part of the system is the deposition chamber where the absorber is fabricated. The deposition chamber is evacuated to the lower part of the high vacuum regime, 10^{-7} mbar, by a Balzer TPU 510 turbo molecular pump, backed by an Edwards E2M40 rotary vane pump. The deposition chamber is connected to a separately pumped load-lock chamber, to simplify loading and unloading.

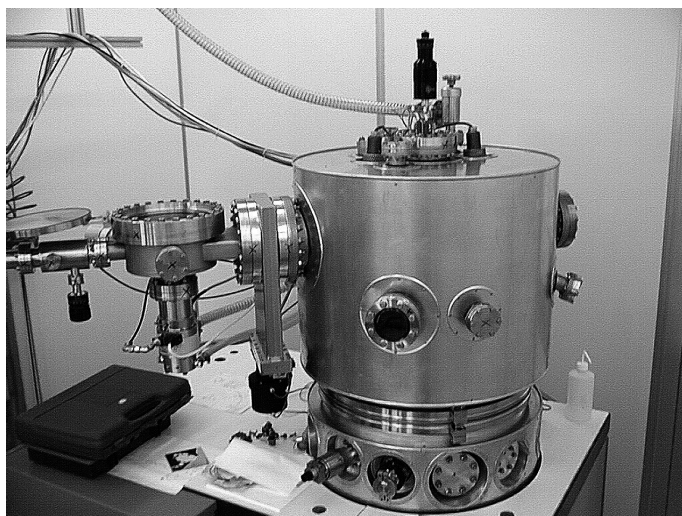


Figure 9: A side view of the deposition chamber, “the UMS”. To the left the load-lock chamber and the linear transfer mechanism is seen. For access to the interior of the chamber, the bell-jar can be lifted via a hydraulic mechanism.

The substrate heater is a stainless steel box equipped with halogen lamps for IR heating, see Figure 10. The substrate is positioned in a substrate holder made of stainless steel, which can be loaded into the substrate heater in the

deposition chamber through a gate valve from the load-lock. The loading as well as unloading is made by a linear transfer mechanism. The halogen lamps in the substrate heater will heat the substrate radiatively from the backside. Two sheathed type K thermocouples are spring loaded to the substrate glass, one in the middle of the substrate, and one in a corner.

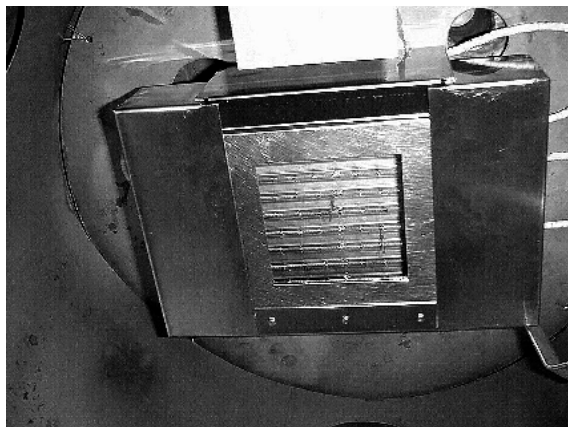


Figure 10: The substrate heater box hanging from the top of the deposition chamber. The substrate is placed in a steel frame which is supported from two sides by the box. The halogen lamps can be seen in the opening in the middle of the box. Between the two halogen lamps in the middle of the heater, one of the thermocouples can be seen, the other is in one of the corners.

The thermocouples are fed through the substrate heater to the substrate between the lamps. Due to the vacuum inside the deposition chamber, the heat transfer to the thermocouples is performed by thermal radiation.



Figure 11: The lower part of the deposition chamber. The three evaporation sources for the metals are fixed on a "cross" which can be tilted for adjustment of the flux of evaporants reaching the substrate. At the lower end of the photo, the simple coil heater for selenium can be seen.

The evaporation sources for copper, indium and gallium are modified Luxel RADAK II sources. In Figure 11 the lower part of the deposition chamber with the evaporation sources is shown. These sources have crucibles of alumina equipped with liners made of pyrolytic boron nitride, PBN. The full charge capacity is about 15 cc, but in order to achieve a more directed evaporation flux, a low filling height is beneficial and for that reason less than 5 cc is normally used.

All sources are equipped with sheathed thermocouples fed from outside the source into a cavity between the source crucible and the source liner. The heat exchange between the source liner and thermocouple is maintained entirely by radiation. Earlier the thermocouples were spring loaded directly against the source liner, but the physical contact in combination with the very high temperature and selenium rich atmosphere led to thermocouple breakdown. The RADAK II evaporation sources used for copper, gallium and indium, have in contrast to modern molecular beam epitaxy sources, no active heating in the uppermost part of the source, the source tip, which thereby becomes colder than the base part of the source. Some of the evaporated metal may therefore condense at the tip, with possible risk for contamination of the molten metal in the source liner as consequence. Also the high selenium content in the deposition chamber is a risk, since it may react with the other metals and/or with source materials to form particles of various compounds that fall into the melt. This, in turn, may change the vapor pressure of the melt, and hence also the evaporation rates. The indium source has an additional problem, as the liquid indium condensed at the tip of the source tends to flow capillary into the heat shield of the source. To reduce this problem the resistant winding that heats the indium source, has been modified so that the upper part of the source is heated more and the lower part less. Since selenium evaporates at a much lower temperature than the metals, a less advanced evaporation source is used for selenium. It consists of a sealed stainless steel tube which contains a resistive heater and a thermocouple. The heater is wound as a coil in the end. The coil holds a quartz crucible where a PBN liner containing the selenium melt is placed.

The evaporation rate of the sources can be controlled by controlling the temperature of the melt. The relationship between source temperature, T , and evaporation rate, r , is approximately following the Equation 5, where A and B are constants.

$$\ln(r) = A + \frac{B}{T} \quad (5)$$

A few words concerning the origin and validity of Equation 5 follows. Based on the *Clausius–Clapeyron relation*[18], showed in Equation 6

$$\ln\left(\frac{p_2}{p_1}\right) = -\frac{\Delta H_{vap}}{R}\left(\frac{1}{T_2} - \frac{1}{T_1}\right) \quad (6)$$

where (p_n, T_n) represent a fixed position in the pressure temperature parameter space, ΔH_{vap} the enthalpy of vaporization for an element and R the universal gas constant. Equation (6) can be rewritten to a more specific form as in Equation 7, called *August Equation* after the German physicist Ernst Ferdinand August (1795-1870).

$$\ln(p) = A + \frac{B}{T} \quad (7)$$

The similarity between Equation 5 and Equation 7 is clear, and only the relation between the vapor pressure of the substances and rate is left in order to justify Equation 5. Since Equation 5 is only to be used in a relatively small interval where desired rates of evaporation are obtained, the relation between the vapor pressure and the actual rate of evaporation for each substance can be interpreted as linear[18], and thus Equation 5 can be expected to be accurate enough to determine evaporation rates based on evaporation source temperatures. This is also what practical experiments show.

In Equation 5, A and B are constants needed to be determined for each individual evaporation source. As discussed above, Equation 5 is an approximation, but is sufficiently accurate in a limited temperature interval. Since the temperature measurement is made by a thermocouple outside the liner containing the melt, there will be an offset between the measured temperature and the temperature in the melt. The determination of the constants A and B is made for each evaporation source individually either by using a quartz-crystal monitor to measure the evaporation rate in situ, or by thickness measurement of the evaporated films afterwards. After calibration, the evaporated flux from each source is controlled by the temperature measured by the source thermocouple.

Between the evaporation sources and the substrate there is a manually controlled shutter. When the shutter is closed it effectively prevents the flux of all metal vapors to reach the substrate. In some cases the shutter is not used, and the evaporation from one single evaporation source is stopped by just turning off the power to that source. In such cases the flux is attenuated gradually, and will sum up to a residual deposition that must be taken into account, especially if the evaporation rate was high before the source was turned off.

3.2 The co-evaporation

In this thesis elemental co-evaporation has been used to fabricate the layers of Cu(In,Ga)Se_2 . Sources containing copper, indium, gallium and selenium in elemental form are heated up individually, to temperatures where they evaporate in a predetermined rate. The total flux, Φ , (atoms per time unit), of the metals leaving each individual source is dependent on the vapor pressure of the metal in the source and the temperature of the melt. The arrival rate of the element to the substrate is dependent on the distribution of the flux and on the distance from the source. The geometrical shape of the evaporation source highly influences the distribution of the flux. As the sources used in this work all have a circular symmetry the distribution from the sources has a form which is described by $\cos^n(\theta)$, where θ is the angle between the normal of the surface of the melt and the direction to an arbitrary point at the substrate. The exponent, n , is a number characteristic for a certain set of source geometry, temperature and element. A higher value of n means a more narrow distribution and subsequently a higher relative maximum rate for the same flux. If the source is directed such that the maximum arrival rate is at the middle of the substrate it follows that the difference in film thickness between the central part of the substrate compared with the outermost part becomes larger. However, the distance between the source and the substrate is large in this work and subsequently the angle (θ) corresponding to the distance between the middle of the substrate and one of the corners is small. Thereby the arrival rate will be rather uniform across the sample. In order to further optimize the uniformity, the sources have been directed at an angle where the maximum flux is away from the middle of the substrate.

Generally, when a metal atom leaves the evaporation source aiming for the substrate, it is not for sure that it will participate in the film growth. Some of the atoms that reach the growth surface may re-evaporate. Other phases may also be formed in the growth that in their turn are evaporated from the surface. The sticking coefficient, S_c [19], shown in Equation 8 describes the ratio of atoms that are used in the formation of the CIGS film and thereby stick to the substrate to all atoms that reach the substrate.

$$S_c = \frac{N_{\text{adsorbed atoms}}}{N_{\text{impinging atoms}}} \quad (8)$$

In our case the sticking coefficients of copper, gallium and indium are expected to be close to one, whereas the sticking coefficient of selenium is lower. Therefore selenium is evaporated in excess in relation to what is needed to form the CIGS film. The deposition rate for each of the elements copper, gallium and indium will therefore in the following be assumed to equal the arrival rate.

The relation between the copper deposition rate per unit area as compared to the indium and gallium deposition rates is given by Equation 9.

$$Y(t) = \Phi_{Cu}(t) / (\Phi_{In}(t) + \Phi_{Ga}(t)) \quad (9)$$

The integral copper concentration in the growing CIGS film, $y(t)$, at a given time, t , in the deposition process equals the time integral of the individual fluxes as in Equation 10.

$$y(t) = \frac{\int_0^t \Phi_{Cu}(t) dt}{\int_0^t \Phi_{In}(t) dt + \int_0^t \Phi_{Ga}(t) dt} \quad (10)$$

A CIGS absorber needs to be slightly copper poor at the end of the process, to ensure the necessary semiconductor properties. This incurs that the elemental ratio of copper atoms to group III atoms, i.e. indium and gallium must not exceed one. For simplicity, the ratio is commonly defined as in Equation 11.

$$y = [Cu] / ([In] + [Ga]) \quad (11)$$

Typically a good functionality for the solar cell is achieved when y is around 0.9 at the end of the evaporation process. Other work has however shown relatively weak dependence of the value of y below 0.9 [20] and the quality of the solar cell. One inherent feature of the elemental co-evaporation process of CIGS is that the growing film undergoes a mixing of the elements during deposition [21]. It is possible to achieve the same final composition of the film with different deposition processes.

3.3 Segregated phase of Cu_xSe

As noted before, the sticking coefficient of selenium is below unity. This incurs that selenium always should be evaporated in excess in order to avoid selenium deficiency in the CIGS layer. At the elevated substrate temperature, typically 500 °C, during deposition, no extra selenium can be incorporated and all excess selenium will be re-evaporated from the CIGS surface.

The chalcopyrite $Cu(In,Ga)Se_2$ material has a relatively wide tolerance for variations of the copper content, y , but only for values of y less than one. For $y < 1$, the electrically neutral complexes with a combination of copper vacancy (V_{Cu}) and indium or possibly gallium atoms at copper sites (In_{Cu}) or

(Ga_{Cu}) will be formed [6]. For values of y larger than unity the excess copper will form a segregated phase of Cu_xSe. This segregated phase, Cu_xSe, has been observed in grain boundaries [22], and on top of the growing Cu(In,Ga)Se₂ layer [23]. When the $Y(t)$ value as defined in Equation 9 exceeds unity, the two phases Cu(In,Ga)Se₂ and Cu_xSe will be formed simultaneously. After cool down, a close to stoichiometric Cu(In,Ga)Se₂ will be found close to the molybdenum layer and on top of this a film of Cu_xSe. As will be discussed later Cu_xSe also segregates to the grain boundaries, but in smaller amounts. For a constant $Y(t)$ value, these two layers will increase their thicknesses proportionally during growth. The two phases have different densities. In paper IX the relation between the corresponding thicknesses of the two phases and the value of the y -value was derived (Equation 12).

$$\frac{d_{Cu(In,Ga)Se_2}}{d_{Cu_xSe}} = \frac{2.1}{y-1} \quad (12)$$

In the example above y equals Y since $Y(t)$ is a constant (constant evaporation rates). During growth at 500 °C the Cu_xSe layer is believed to be in a semi-liquid state [21]. The mobility of all elements is high in the semi-liquid Cu_xSe medium, which leads to rapid interdiffusion and may facilitate grain growth. This growth is referred to as *Vapor-Liquid-solid* growth mechanism [24]. Generally, films grown under copper rich conditions $Y>1$ such that the y -value is kept above unity, i.e. in the presence of Cu_xSe, have significantly larger grains than those grown copper poor (with $Y<1$ at all times). In many CIGS recipes a combination of copper rich and copper poor growth conditions is therefore used, but always with a copper poor final composition ($y<1$).

3.4 Radiative properties of CIGS during growth

When the substrate is heated by the substrate heater it dissipates power, P , by thermal radiation. The amount of power lost this way is determined by Stefan-Boltzmann law, Equation 13,

$$P = \sigma \cdot T^4 \cdot A \cdot \varepsilon \quad (13)$$

where σ is the Stefan-Boltzmann constant equal to $5.67 \times 10^{-8} \text{ W}/(\text{m}^2\text{K}^2)$, T is the surface absolute temperature, A is the substrate area and ε the surface emissivity. For a so called black body, i.e. a body for which the surface emissivity is constant and equal to one, the spectral irradiance, $M_{\lambda,b}(\lambda, T)$, given by Planck's law of radiation (Equation 14), is shown in Figure 12.

$$M_{\lambda,b}(\lambda, T) = \frac{2\pi h c_0^2}{\lambda^5 \left(e^{\frac{hc_0}{\lambda k_B T}} - 1 \right)} \quad (14)$$

In Equation 14, h is Planck's constant equal to 6.6262×10^{-34} Js, c_0 is the speed of light in vacuum equal to 2.9979×10^8 ms⁻¹ and k_B the Boltzmann constant equal to 1.3807×10^{-23} JK⁻¹.

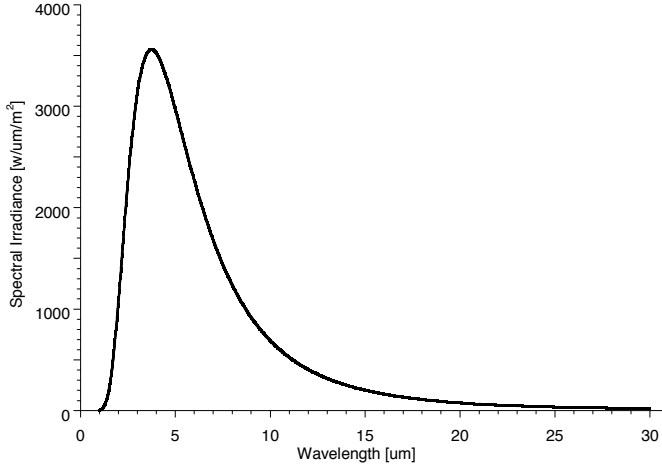


Figure 12: Spectral irradiance for a black-body radiator at 500 °C.

After heating up the substrate, but before opening the shutter to the evaporation sources, i.e. just before the deposition of the film starts, the thermal radiation from the substrate is given by the emissivity of molybdenum alone. Molybdenum is optically opaque for all wavelengths relevant to thermal radiation and therefore the influence of the soda-lime glass substrate on the radiation from the surface can be disregarded.

When the shutter is opened and a film is starting to grow on the molybdenum coated substrate, the emissivity will change. If a copper poor CIGS layer is grown, the emitted radiation will be governed by the emissivity of a growing stoichiometric Cu(In,Ga)Se₂ layer on top of the Mo layer. If instead a copper rich CIGS is grown, the emissivity of the substrate is given by the optical stack composed of growing Cu_xSe/growing stoichiometric Cu(In,Ga)Se₂/molybdenum. As was shown in paper IX, the emissivity of the stack will be governed by the bulk emissivity of Cu_xSe alone if the thickness of the Cu_xSe layer is sufficient, since it then becomes optically opaque.

The surface temperature is not exactly known, since the temperature control is performed by a thermocouple at the backside of the 1 mm thick soda

lime glass substrate, but is believed to be sufficiently close to the thermocouple temperature. The CIGS film growth in the scope of this thesis has always been under a constant set value for the substrate temperature (500 °C). Typical values of emissivity for copper rich and copper poor CIGS was in paper IX found to be about 0.4 and 0.1 respectively. The area of the substrate is 0.01 m². The radiated power according to the Stefan-Boltzmann law is thereby 90 W for copper rich CIGS and 20 W for copper poor.

3.5 The use of End-Point-Detection

Based on the fact that there is an emissivity change going from copper rich to copper poor CIGS bulk composition or vice versa, a control method called End-Point-Detection, EPD, can be used to monitor the film composition during the deposition process.

The company Matsushita Electric reported to use this method 1994 to monitor the copper concentration in CIS and CIGS films [25,26,27]. The principle they used was to heat the substrate with the substrate heater under constant power. Then they monitored the temperature change of the substrate caused by a change in emissivity of the film, as the copper concentration of the CIGS film evolved from copper poor to copper rich and finally back to copper poor composition.

In the experimental work for this thesis, most of the depositions have been performed using the opposite strategy. The substrate temperature has been kept constant, and the electrical power fed to the substrate heater has been monitored. In Figure 13, a flow chart of how the temperature feed back loop operates is shown. A thermocouple reading the substrate temperature gives feedback to a PID-controller. The PID-controller which is set to maintain a constant set temperature, controls an electric power supply which in turn feeds the substrate heater lamps.

The substrate temperature as measured at the backside of the substrate is constant during the entire process. The surface temperature will be lower for a higher emissivity, but since the thickness of the glass is only 1 mm, the difference is small. The change in surface emissivity is however large when the transition from copper rich to copper poor CIGS, or vice versa occurs in the growth process. This will lead to a change in electrical output power to the substrate heater. The output power is therefore a useful control parameter for monitoring if the film is copper poor or copper rich. To conclude, a copper poor CIGS film contains no Cu_xSe and for that reason has a low emissivity leading to low output power to the substrate heater. In contrast, a copper rich CIGS film contains Cu_xSe and consequently a higher emissivity leading to higher output power to the substrate heater to maintain 500 °C.

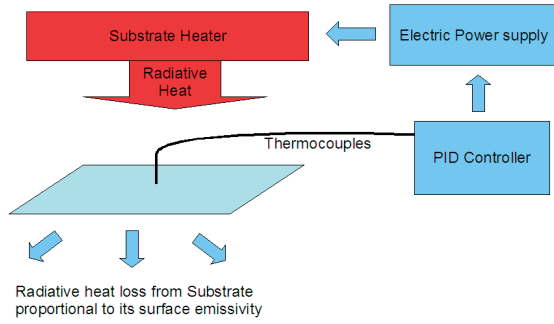


Figure 13: A flow chart of the feed-back loop for the control of the constant set temperature of the substrate.

3.6 The two-stage CURO deposition process

In the experimental work for this thesis most of the CIGS layers have been co-evaporated according to a two-stage growth process, described in detail in paper I and II and also discussed in paper III and V. A brief description is given below. In Figure 14 a graph of a typical CURO process is shown.

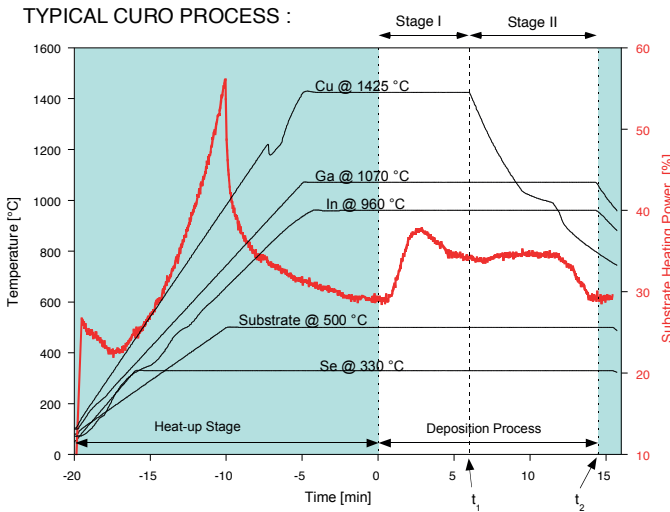


Figure 14: A diagram showing the temperature of the deposition sources and the substrate heater as well as the electrical output power to the substrate heater.

During the entire CURO process, the substrate is kept at 500 °C. The selenium flux with an overpressure of around a factor of 1.5 as compared to the stoichiometric needs is also kept constant (by keeping the selenium source at a constant set temperature of 300 °C). In the first stage, copper, indium and gallium are evaporated with deposition rates corresponding to $Y > 1$, and

thus the growing CIGS film is copper rich with $y > 1$. Consequently, Cu_xSe is formed together with a close to stoichiometric layer of $\text{Cu}(\text{In,Ga})\text{Se}_2$. At the end of the first stage, according to $t = t_1$ in Figure 14, the copper source is turned off, and the evaporation rate of copper decreases rapidly. In the second stage between t_1 and t_2 in Figure 14, only indium and gallium are evaporated together with selenium. As can be seen in Figure 14 the set temperatures of the indium and gallium sources are unchanged in the second stage and thus also the deposition rates. As a consequence, the y -value decreases. During this stage, the $\text{Cu}(\text{In,Ga})\text{Se}_2$ is still growing, consuming the Cu_xSe layer as an internal source of copper. As the amount of Cu_xSe decreases below a critical level, the emissivity starts to decrease and thus less power is needed to maintain a constant substrate temperature as can be seen in Figure 14. When no Cu_xSe is left, the $\text{Cu}(\text{In,Ga})\text{Se}_2$ film is stoichiometric and $y = 1$. At this point the emissivity has reached a low value. Since the deposition rates of indium and gallium are maintained for some time after the point of stoichiometry is reached the final y -value of the CIGS film will be lower than unity. The deposition process is finished at $t = t_2$ when $y \approx 0.9$ and the shutter is closed manually. The excess of indium and gallium atoms will not be permanent at the CIGS surface, rather will copper atoms be distributed within the CIGS film by out-diffusion from the bulk to the surface during the final stage of the growth [28,29].

This process recipe has been given the acronym CURO, which shall be understood as “first **Cu-rich** then **Cu-source off**”. The origin of the CURO process is from the Boeing Aerospace Company [30,31], and was used for fabrication of CIS rather than CIGS. The CURO process is an extreme variant of the original recipe since the copper deposition rate in the second stage of CURO is zero whereas the Boeing process decreases the deposition rate of copper such that $Y < 1$, but only slightly, leading to a more gentle decrease of y .

The evaporation rate, Φ , from the sources in the CURO process can be expressed with help of Heaviside's step function, $\theta(t)$, as in Equation 15,

$$\Phi_{\text{Cu}}(t) = r_{\text{Cu}} \cdot [\theta(t) - \theta(t - t_1)] \quad (15a)$$

$$\Phi_{\text{In}}(t) = r_{\text{In}} \cdot \theta(t) \quad (15b)$$

$$\Phi_{\text{Ga}}(t) = r_{\text{Ga}} \cdot \theta(t) \quad (15c)$$

where r is the constant rate from a source when it is active, $\theta(t)$ is 0 for $t < 0$ and 1 for $t > 0$. The concentration of copper, $y(t)$, at a certain time, t , in the second stage can then be calculated using Equations 8 and 13 as in Equation 16, where t_1 is the time when stage 1 ends.

$$y(t) = t_1 y(t_1) \cdot \frac{1}{t} \quad (16)$$

Consequently, if a measurement of the y -value is made for a deposited CIGS sample, the copper concentration during the first stage can then be calculated according to Equation 17, where t_2 is the time at the end of the deposition.

$$y(t_1) = \frac{t_2}{t_1} y(t_2) \quad (17)$$

To monitor the deposition process, the electrical output power (OP-signal) to the substrate heater is being observed and recorded. As can be seen in Figure 14, the OP-signal stabilizes at roughly a constant high level, after an initially even higher peak. The final state of the growth is seen as a decrease in the OP-signal as the CIGS material undergoes the change from copper rich to copper poor to reach a constant low value as discussed above; the endpoint detection. As soon as a convincing lowest value of the OP-signal is seen, the shutter is closed.

In paper I a study was made, to compare the OP-signals from a short (15 minutes) and a long (45 minutes) CURO deposition, seen in Figure 15. Since the shape of the two curves did not differ, the conclusion was that the thermal dynamics of the equipment is fast enough to assure a steady state relationship between the OP-signal and the actual composition of the growing film. Solar cells fabricated from these CIGS films showed only a small difference in quality in spite of large differences in film formation time. The electrical conversion efficiency for the solar cells fabricated from CIGS grown by the short and long recipe were 14.7 % and 15.6 % respectively.

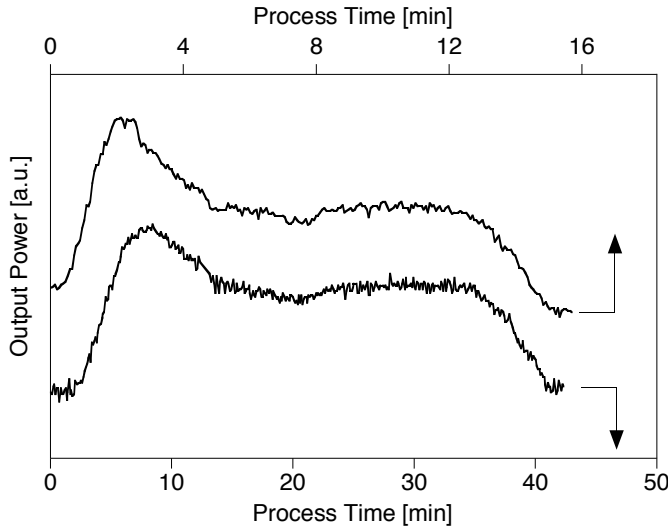


Figure 15: A comparison of the OP-signal from a short and a long CURO process. Since the shapes of the OP-signal curves are nearly identical, the conclusion is that the dynamics of the system are faster than the emissivity change.

In paper II, variations of the t_1 / t_2 ratio for the CURO process during the first stage were implemented, see Figure 16. The resulting conclusion was that the degree of copper excess did not influence the electrical conversion efficiency of the solar cells significantly, see Table 1. From a morphological point of view, a clear difference could however be seen.

Table 1: Characteristics for solar cells fabricated with CIGS film grown by different recipes.

Process Device	t_1/t_2	V_{oc} [mV]	J_{sc} [mA/cm ²]	FF [%]	η [%]
"5+10"	1/3	575	33.7	68.0	13.2
"10+5"	2/3	581	34.4	8.7	13.7
"13r+2"	13/15	589	31.5	72.2	13.4
"13p+2"	13/15	549	31.5	71.7	12.4
CUPRO	—	579	35.6	71.1	14.7

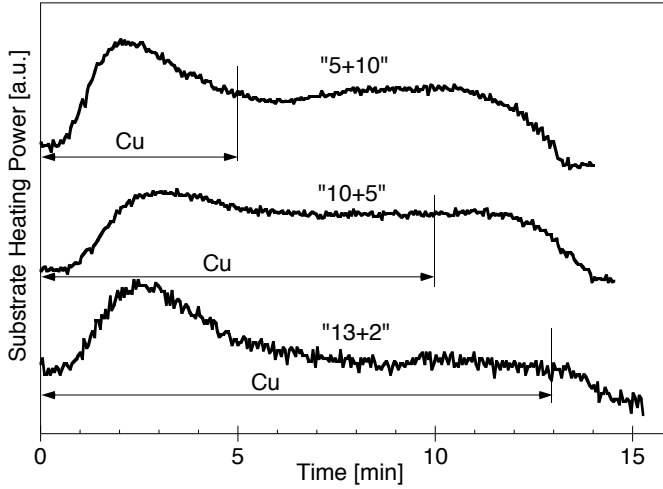


Figure 16: The OP-signal for different t_1 / t_2 ratio for the CURO process.

CIGS films with a final y -value below unity, that have been very copper rich in the first stage, often exhibit deep crevices, as can be seen in Figure 17, sometimes from the surface down almost to the back contact. The depth of crevices can roughly be correlated to the fraction of the time of the first stage, t_1 , to the total deposition time, t_2 .

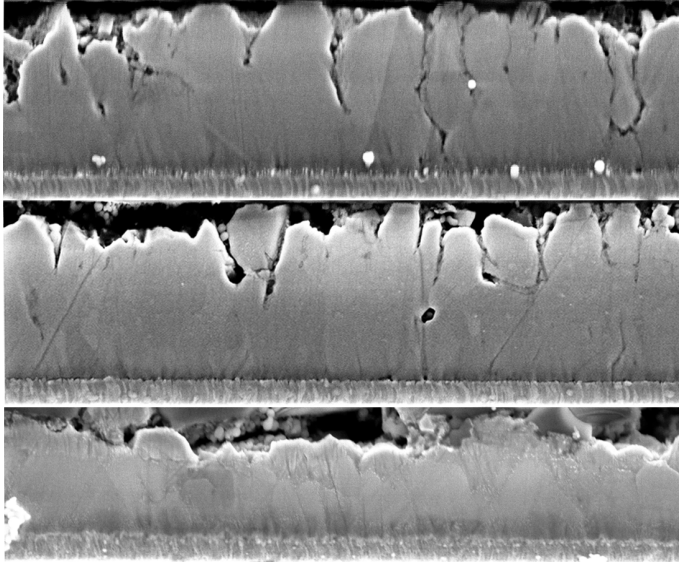


Figure 17: Cross-section SEM images of polished CIGS films. Top: CURO process with $t_1/t_2=1/3$. Middle: CURO process with $t_1/t_2=2/3$. Bottom: Only the first stage of a CURO process.

The most probable explanation to the crevices is that a fraction of the segregated Cu_xSe phase during the copper rich stage of the process has been located in between the growing $\text{Cu}(\text{In,Ga})\text{Se}_2$ grains. After the copper source has been turned off in the second stage, intragrain Cu_xSe is used as an internal copper source and since copper is a highly mobile atom, copper has been moving out of the grain boundaries rather than indium and gallium into the grain boundaries.

An interesting phenomenon occurred for the deposition referred to as “13+2”, seen in Figure 16. Due to the alignment of the evaporation sources in the vacuum chamber, there is always a slight gradient in y -value across the substrate. Since the copper deposition rate was comparably low for a CURO process during the first stage in the “13+2” deposition, some part of the substrate has actually never been copper rich. A clear border could visually be seen on the sample, between the part which was copper rich in the first stage, and the part which was not. These films denoted “13+2r” and “13+2p”, (r and p denotes rich and poor respectively) were analyzed with x-ray diffraction, XRD. The texture of the two CIGS films showed to be completely different. The “13+2r” exhibited a strong (112) texture, which was expected as coming from a CURO process [32,33]. The “13+2p” on the other hand was instead oriented as (220), (204). This result is coherent with theories concerning copper deficient CIGS growth published earlier [24,34]. Scanning electron microscope, SEM, analysis also showed a much smoother top surface of the “13+2p” sample along with significant smaller grains than the “13+2r” sample.

3.7 The three-stage process CUPRO

After the special “13+2” CURO deposition an idea led to the modification of the recipe to contain a copper rich flux in the middle of the process [35], see paper II. This recipe, which has three stages, combines the “13+2p” process for crevice free, smooth material with the endpoint detection usable CURO process for large grains. In the first stage of this three-stage deposition process the CIGS is grown under slightly copper poor conditions with all deposition rates constant in the first stage. Ideally most of the CIGS material is deposited in this stage. Hereby the cause for the formation of crevices of the CURO process is avoided. In the beginning of the second stage the temperature of the copper source is ramped up to a higher temperature, leading to an increased deposition rate of copper and a Y-value exceeding unity. When The CIGS becomes stoichiometric, no more copper can be accommodated in the Cu(In,Ga)Se_2 film and a segregated phase of Cu_xSe starts to form. This leads to an increase of emissivity and a related increase of the OP-signal as seen in Figure 18. At the end of the second stage the copper source is turned off as in the CURO process, and the overall copper content, y , decreases during the third stage. The end of the process is reached when $y \approx 0.9$. At this point the OP-signal has reached a stable low value. This process is referred to as CUPRO, (**Cu**-poor, then **rich**, then **Cu source off**).

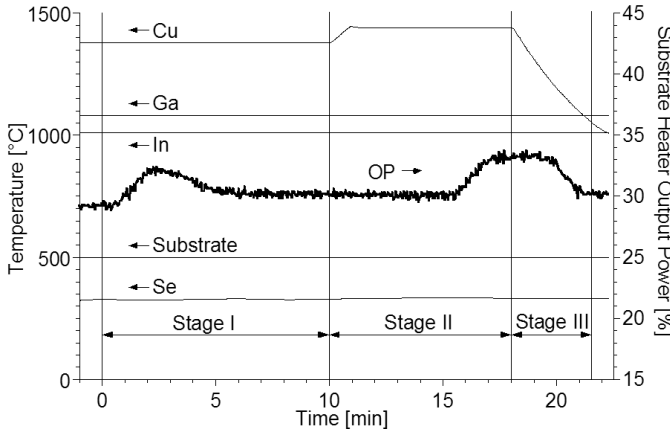


Figure 18: Graph showing the source and substrate temperatures and the OP-signal to the substrate heater for a CUPRO process. The level of the OP-signal in the first stage, after the initial bump is just slightly higher than the level for $t < 0$ due to the low emissivity for copper poor CIGS. At the end of the second stage, Cu_xSe segregates as the y -value exceeds one and the OP-signal reaches a higher level. In the third stage the OP-signal returns to a low level as the Cu_xSe is being consumed.

The OP-signal for the CUPRO process, seen in Figure 18, can be described as follows: In the first stage as the shutter is opened, the growing of a copper deficient Cu(In,Ga)Se_2 layer creates a peak behavior similar to the CURO process. This has been found to be due to an emissivity maximum for a cer-

tain thickness of Cu(In,Ga)Se_2 on top of the highly reflective molybdenum layer, see paper IX. Since according to Kirchhoff's law in Equation 18,

$$R + A + T = 1 \quad (18)$$

where R is reflectance, A is absorptance which is equal to emittance during steady state conditions, and T is transmittance, and as has been mentioned earlier, $T = 0$ due to the opaque molybdenum layer, the reflectance can be written as in Equation 19.

$$R = 1 - \varepsilon \quad (19)$$

The thin layer of growing Cu(In,Ga)Se_2 is consequently passing a state where it acts as an anti-reflective layer. After the peak behavior, the OP-signal stabilizes at a nominally constant level typical for copper poor CIGS. In the second stage the OP-signal is unchanged until the Cu_xSe has started to segregate, after which it starts to increase. A new stabilized high level, equivalent to that of the first stage in the CURO process is finally reached, followed by a decrease down to the low copper poor level again at the end of the third stage.

In paper IV, a study of the influence of substrate temperature for the Cu(In,Ga)Se_2 films made by the CUPRO process was made. Four different temperatures were used: 475, 500, 525 and 550 °C. Solar cells made of the Cu(In,Ga)Se_2 films all exhibited good electrical conversion efficiency, but $\text{QE}(\lambda)$ measurements showed a decrease of bandgap for higher temperature. This may be an effect of an increased non uniform distribution of the Ga/(Ga+In) ratio with increasing temperature. This would explain the result above since $\text{QE}(\lambda)$ measures the lowest bandgap in a distribution.

XRD measurements showed three significant trends linked to the substrate temperature. First a gentle trend of increased (112) orientation compared to (220)(204) orientation with higher temperature. Secondly, the increased temperature seems to shift the peak to lower angles caused by lower gallium content. Thirdly, for the peaks (116)(312) and slightly less, (220)(204) a peak splitting becomes more pronounced as the temperature is increased, indicating more In/Ga inter mixing at higher temperature.

3.8 The INRO process

With the goal to gain more knowledge of the re-crystallization of the Cu(In,Ga)Se_2 grains, attempts were made in paper VII to use a growth process with initial copper poor composition followed by a conversion to copper rich, i.e. the opposite to the CURO process. It is thus a two-stage deposition process. Another goal with this process was to avoid the deep crevices achieved as a consequence of copper rich growth in CURO process.

In the first stage a Cu-poor CIGS is grown ($y < 1$), with constant fluxes for all evaporation sources ($Y < 1$) and the substrate held at 500 °C. The CIGS layer thus grows as in the first stage of the CUPRO process. At the time the second stage starts, both the indium and the gallium sources are turned off. During this stage the composition with regards to copper content (y), will gradually become less and less Cu-poor. This process become denoted INRO as “**In**-rich then In-source **off**”. In Figure 19 is shown how the OP-signal evolves during a INRO process. The evaporation flux during the entire deposition process can be expressed as Equation 20.

$$\Phi_{Cu}(t) = \Phi_{Cu} \cdot \theta(t) \quad (20a)$$

$$\Phi_{In}(t) = \Phi_{In} \cdot [\theta(t) - \theta(t - t_1)] \quad (20b)$$

$$\Phi_{Ga}(t) = \Phi_{Ga} \cdot [\theta(t) - \theta(t - t_1)] \quad (20c)$$

Then the copper composition, $y(t)$ during the second stage is given with Equations 8 and 18 as in Equation 21.

$$y(t) = \frac{y(t_1)}{t_1} \cdot t \quad (21)$$

In paper VII, three CIGS films fabricated with the INRO process are being analyzed. In Figure 19, the positions (striped lines) in the second stage where the depositions were interrupted are shown.

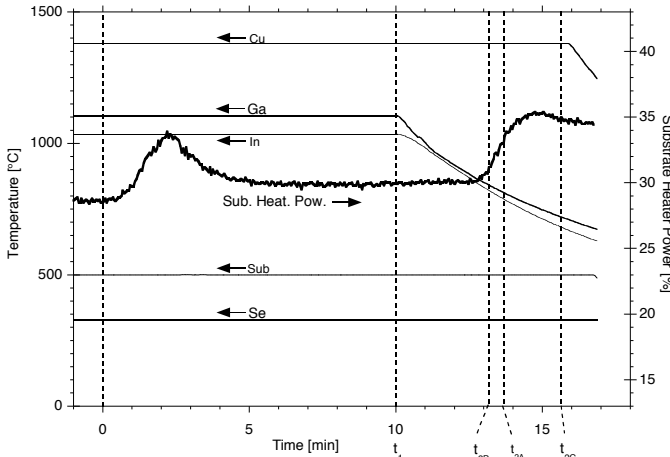


Figure 19: A graph showing the source and substrate temperature and the OP-signal for the substrate heater of an INRO process.

Due to the inherent gradient of the copper composition caused by the source alignment described in section 3.6 , the deposition with the smallest increase of y , (denoted B) was made such that when the visible increase in the OP-signal occurred due to formation of Cu_xSe , there were parts of the substrate that were still copper poor.

Analyses with energy dispersive X-ray spectroscopy, (EDS), on sample B gave values of copper content, y , equal to 0.87, 0.96 and 1.05 for the most copper poor, the middle and the most copper rich positions respectively. Images by scanning electron microscopy seen in Figure 20, of the two extreme positions show how a grain enlargement occurs when the copper poor CIGS is brought to copper rich.

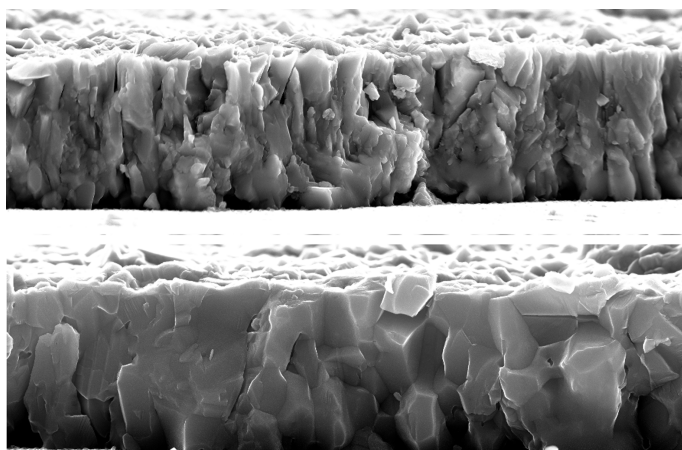


Figure 20: SEM images of CIGS films from same deposition. Both films have a thickness of 2 μm . Due to evaporation source alignment, a gradient in copper concentration is evident on the film. Top: copper poor CIGS with small grains. Bottom: copper rich CIGS, where the grains have been enlarged.

3.9 The constant power mode

Instead of keeping the substrate at a fixed temperature and monitoring the OP-signal, endpoint detection can, as already mentioned [25,26,27] be used reversibly. In that case the output power to the substrate heater is fixed to a value that is known to generate a suitable substrate temperature. When the copper content, y , of the CIGS passes the value $y = 1$ from either direction a change in emissivity occurs leading to a corresponding change in substrate temperature, which then is monitored. This method has been used by other research groups with successful results.

In a comparison between substrate heating by constant temperature and by constant power, it is evident that the speed of dynamics is much lower for the strategy with constant power. In Figure 21 a graph depicting a deposition with constant power is shown. The deposition is performed according to CURO. In Figure 21 five regions are indicated (A-E), which are discussed in the following. In region A before any deposition has occurred, the emissivity of the substrate is constant and given solely by the emissivity of molybdenum. The increase in measured temperature of the substrate is due to increased temperature of the substrate heater, which is a dynamically slow process. If sufficiently long time would have been used in the heating stage, thermal steady state would have caused virtually constant temperature. Experiments with the UMS system has shown that roughly one hour is enough.

In region B, when the shutter has been opened, the emissivity is rising ($d\varepsilon/dt > 0$) following the first stage of the CURO process, described in chapter 3.6, and the temperature is therefore decreasing. This continues almost linearly until the trend is broken when a maximal emissivity is reached ($d\varepsilon/dt = 0$) in region C. Even though the temperature signal in B, appears to be linear, the reason is not trivial. The curve is composed of firstly a non constant $d\varepsilon/dt$, and secondly, a varying difference between the actual substrate temperature and the substrate temperature of a steady state condition with the actual emissivity, i.e. in a situation where the dynamics of the system were sufficiently rapid.

In region C the temperature is however still decreasing apparently linearly, but with another slope, compared to B. The mechanism for the behavior in C is the power to attain thermal steady state for the system as in A, but in the opposite direction, i.e. with decreasing temperature. The difference in achieved substrate temperature between just molybdenum and a sufficiently thick Cu_xSe layer (copper rich CIGS) to dominate the emissivity, cannot be concluded from Figure 21 since none of the regions, (A or C), has reached thermal equilibrium.

In region D, again as in B, two features add up to form a driving force for the temperature change. First the non constant $d\varepsilon/dt$ which now is negative in comparison to B, and second the approach for the system to reach thermal steady state. Also a contributing factor but of second order is the cooling of the copper evaporation source. Other experiments have shown a detectable but very small power increase for the substrate heater when running in constant temperature mode, when the copper source is being shut off.

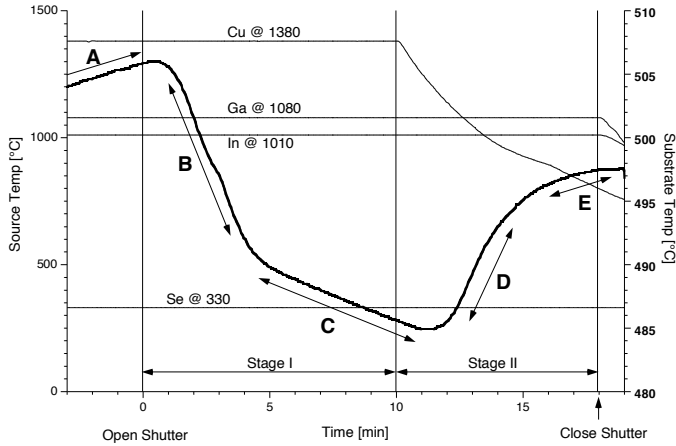


Figure 21: The thick line represents the substrate temperature during a CURO deposition process in constant power mode. Description of the different process regions: A: Temperature increase to reach steady-state. B: Decrease in temperature caused by increased emissivity and changed thermal situation. C: The emissivity is constant, and the temperature would, in a steady-state situation, have been constant. D: Decrease of emissivity causes an increase of substrate temperature. E: The emissivity is constant, but slow thermal dynamics hinder a constant substrate temperature.

In region E the only driving force for the temperature change is the reaching of thermal equilibrium for the equipment. It is obvious from Figure 21 that a well defined boundary between region D and E is hard to detect. For that reason the use of the end-point detection control as a method for accurate film composition is not very useful in this case. If, however, measurements of film emissivity is performed with a two color pyrometer [36], a change in emissivity would be detectable even under the circumstances that the substrate temperature also changes.

In paper VI a coarse model was used to simulate the temperature of the substrate during a CURO process. In the model a substrate heater was given parameters such as consumed power, mass, emissivity, thermal conductivity and thermal capacity. A substrate was also defined by various thermal properties. Between the heater and the substrate, a thermocouple was placed. Since the thermocouple was not in thermal contact with the substrate, the thermal flow between substrate heater, thermocouple and substrate was only due to thermal radiation. A picture of the geometry is seen in Figure 22. The time lag due to thermal conduction in the thermocouple was taken into account by letting the thermal junction be on different positions (A-D) from the substrate.

The simulation was implemented with FEMLAB™, which uses the finite element method. In the work for the article, the model was refined continuously. Finally the simulation succeeded in showing thermal behavior for the substrate very close to what was achieved experimentally, see Figure 23.

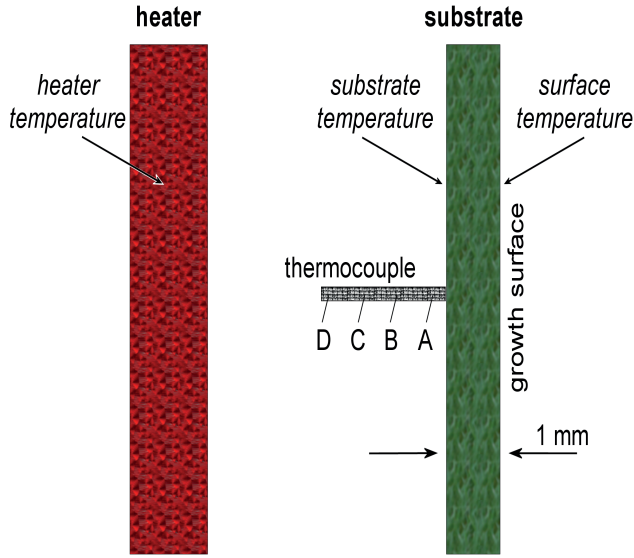


Figure 22: The geometry of the part involved in the FEMLAB™ simulation. The indications A-D on the thermocouples symbolize where inside the sheathed thermocouple the junction is placed.

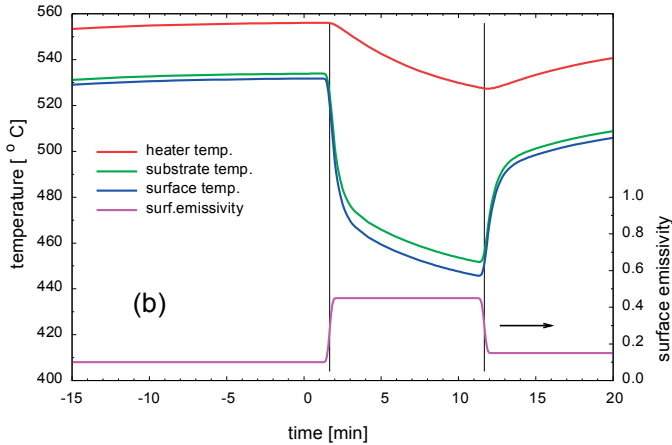


Figure 23: Simulation of the temperatures of substrate heater, backside of the substrate and of the front side due to emissivity changes of the front side. The emissivity change between different stages of the simulated growth process is implemented by error functions as in Equation 22. Qualitatively a very good agreement of simulated and measured substrate temperature is found in a comparison with Figure 21.

In the simulation, error functions, seen in Equation 22, with variable time constants were used for the transitions between the constant emissivity for molybdenum/copper rich CIGS/copper poor CIGS.

$$\varepsilon(t) = \varepsilon_0 + \frac{\varepsilon_1 - \varepsilon_0}{2} \left[1 + \operatorname{erf} \left(\frac{t - t_1}{\tau_1} \right) \right] + \frac{\varepsilon_1 - \varepsilon_1}{2} \left[1 + \operatorname{erf} \left(\frac{t - t_2}{\tau_2} \right) \right] \quad (22)$$

This is a simplification which gives smooth transitions but suffers from lack of knowledge about the emissivity in the phase transitions. A new simulation today with information from papers VIII and IX should have potential to give results even more close to reality than in paper VI.

4. Simulation of the growth process

After many depositions of CIGS films with the UMS system, it is evident that the OP-signal is governed not only by the growing film, but also by parameters linked to the equipment, as unsatisfying temperature readings by the thermocouples, slow thermal dynamics caused by thermal mass et cetera. For such reasons, it is of interest to study the radiative properties of the growing CIGS film with a method decoupled from the influence of the deposition system. For example, the peak behavior of the OP-signal in the beginning of all processes mentioned in chapter 3 was interpreted as an artifact caused by the PID controller, a typical overshoot. In this chapter simulations of the film growth will be discussed, showing that the peak behavior of the OP-signal is actually caused by the emissivity of the growing film. Another area of interest is the OP-signal behavior for copper rich CIGS with a decreasing layer of Cu_xSe on top. In some depositions with CURO or CUPRO processes a peak of the OP-signal before the CIGS becomes copper poor has been observed. This has been proven to be real characteristics of the film caused by changes in the emissivity due to variations in the thickness of the Cu_xSe layer.

4.1 The optical model

The radiation from the substrate is determined by the emissivity of the optical stack: $\text{Cu}_x\text{Se}/\text{Cu}(\text{In,Ga})\text{Se}_2/\text{Mo/glass}$. To link the material properties of the individual materials in the optical stack, with a macroscopic property such as emissivity, an optical model was used. The optical model describes the optical response in terms of reflectance, R , and transmittance, T , for an optical stack with light incident to it. The origin of the optical model used in this thesis comes from Pfrommer et al [37], and was implemented to a computer simulation program in MATLAB™ by J. Malmström [13]. A flow chart describing input and output parameters are shown in Figure 24. In this thesis no attempts will be made to describe the optical model in detail, rather it is used as a “black box”-tool.

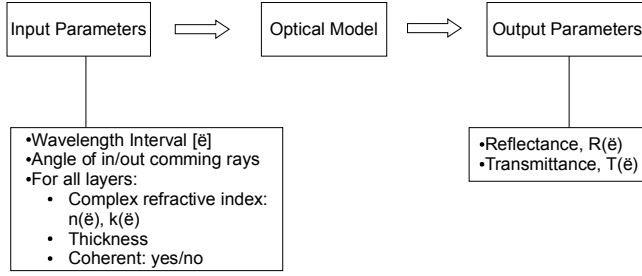


Figure 24: A flow chart describing input and output parameters for the optical model.

To be able to use the optical model, the optical constants for all involved materials must be known.

4.2 Determination of the optical constants for CIGS and Cu_xSe

Optical constants are quantities which are unique for each material. They are generally not influenced by geometry or size, as long as the size in all directions exceeds a few nanometers (such that quantum size effects can not be seen [38]), but are functions of the wavelength. The optical constants are usually represented by either the complex refractive index as in Equation 23,

$$N = n + ik \quad (23)$$

or by the complex dielectric constant (Equation 24).

$$\tilde{\epsilon} = \epsilon_1 + i \epsilon_2 \quad (24)$$

The relation between the complex refractive index and the complex dielectric constant is given in Equation 25,

$$\tilde{\epsilon} = N^2 \quad (25)$$

or separated into real and imaginary parts as in Equation 26.

$$\epsilon_1 = n^2 - k^2 \quad (26a)$$

$$\epsilon_2 = 2nk \quad (26b)$$

For CIGS, published data of n and k were found for wavelengths from 0.3 μm up to 2.5 μm [39]. This interval corresponds well to the solar spectrum and these data are needed to model the behavior in the relevant interval for absorption of sunlight, see Figure 2. For Cu_xSe no data at all was found. In order to correctly model the behavior of $\text{Cu}(\text{In,Ga})\text{Se}_2$ and Cu_xSe for heat radiation the refractive indices in long wavelengths from 2 μm to 20 μm need to be known. This is discussed in the following.

The method used to determine n and k was by combined transmittance and reflectance measurements on optical stacks consisting of a substrate and a film. For each wavelength the measured quantities R_{measured} and T_{measured} should equal the quantities $R_{\text{calculated}}$ and $T_{\text{calculated}}$ which were calculated using the optical model. The calculated quantities are functions of several parameters as shown in Equation 27.

$$R_{\text{stack, measured}}(\lambda) = R_{\text{stack, calculated}}(\lambda, N_{\text{sub}}, N_{\text{film}}, d_{\text{film}}, d_{\text{sub}}) \quad (27a)$$

$$T_{\text{stack, measured}}(\lambda) = T_{\text{stack, calculated}}(\lambda, N_{\text{sub}}, N_{\text{film}}, d_{\text{film}}, d_{\text{sub}}) \quad (27b)$$

In Figure 25, the optical stacks are shown and how the optical measurements are performed on them.

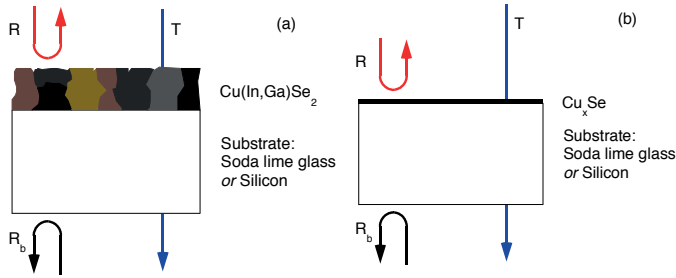


Figure 25. The optical stacks used for determination of the optical constants for: a): $\text{Cu}(\text{In,Ga})\text{Se}_2$ and b): Cu_xSe . Three types of optical measurements were made with spectrophotometer on each optical stack: Reflectivity on the front side (R), reflectivity on the back side (R_b) and transmissivity (T). All measurements were made in specular mode.

The role of the substrate is only to physically support the thin film during the optical measurements. Ideally, optical measurement on the thin film alone would be superior, but is not possible to perform in practice. The choice of substrate for this study is worth a short comment. Soda lime glass substrates are normally used for growth of CIGS films and is the natural choice if relevant CIGS material is to be studied. A drawback with this kind of substrate is however its limited transmittance for infrared radiation. Above 4.5 μm soda lime glass is opaque. Highly resistive silicon substrates are sufficiently

transparent (about 50 % transmittance) in the entire wavelength interval, but were unfortunately not inert enough. As is discussed in paper VIII, the diffusion of copper in silicon at 500 °C and probably subsequent formation of copper silicides caused a rough interface between the CIGS film and the silicon substrate. The same is likely to have occurred for the Cu_xSe film on the Si substrate. In order for the optical model to be applicable, all interfaces must be optically smooth such that no light is diffusely scattered. The spectrophotometer Lambda900 is capable of measuring reflectivity and transmissivity of both diffused and specular light. It was evident that the CIGS films, as grown, on both the soda-lime glass and the silicon substrate reflected light diffusely in the wavelength interval from 0.3 μm to 2.55 μm . For the samples with Cu_xSe this could not be seen. The CIGS samples were for that reason polished with diamond polish (1 μm), until no diffuse component of the reflections could be seen for wavelengths shorter than approximately 1 μm .

Above this range the band gap of silicon (1.12 eV which corresponds to a wavelength of 1.11 μm) the reflection had a diffuse component. This indicated a diffusive scattering interface between the $\text{Cu}(\text{In,Ga})\text{Se}_2$ film and the silicon substrate. The diffuse component is however decaying for longer wavelength, and is negligible above 5 μm .

To reduce the number of unknown variables in Equations 27a and b, the optical stack is first reduced to contain only the substrate alone. Reflectance and transmittance are measured for the substrate only, and Equations 28 are solved.

$$R_{\text{sub,measured}}(\lambda) = R_{\text{sub,calculated}}(\lambda, n_{\text{sub}}, k_{\text{sub}}, d_{\text{sub}}) \quad (28a)$$

$$T_{\text{sub,measured}}(\lambda) = T_{\text{sub,calculated}}(\lambda, n_{\text{sub}}, k_{\text{sub}}, d_{\text{sub}}) \quad (28b)$$

The solutions of Equations 28 are dependent on that the thicknesses for the substrates are known (525 μm for the silicon and 1000 μm glass substrate respectively). As will be seen, a complication when using the solution is however that the inversion of the equation system Equations 28, is multivalued, and not analytically solvable (Equations 29).

$$n(\lambda) = n(\lambda, R, T) \quad (29b)$$

$$k(\lambda) = k(\lambda, R, T) \quad (29b)$$

In order to find solutions for n and k that satisfy Equations 28, a numerical method is used. An nk -space is chosen “sufficiently” large to ensure that the true physical solutions for n and k are found within the space. A mesh with sufficient resolution is applied on the space. For every node in the mesh (n_i ,

k_j), Equations 28 are solved. The result will be traces (so called iso-lines), in the nk -space for both $R(n,k)$ and $T(n,k)$ where Equations 28 are satisfied. The intersections of the iso-lines for R and T are solutions of the equation system Equations 28. This method has been used by several groups [40,41,42].

In the case of the determination of n and k for the silicon and glass substrates, the physical solutions were easy to discern since, in cases of multiple solutions, only one was physically reasonable. With known optical constants for the silicon and glass substrates, the equation system (Equations 27) for the optical stacks composed of Cu(In,Ga)Se_2 /(silicon or glass substrate) and Cu_xSe /(silicon or glass substrate) respectively, was also possible to solve.

Figure 26 shows the intersections between iso- R , iso- T and iso- Rb for an optical stack composed of Cu(In,Ga)Se_2 /glass. The thickness of the Cu(In,Ga)Se_2 film provided for the calculation was $1.44 \mu\text{m}$, and the wavelength $3.0 \mu\text{m}$. In a) the nk -space is very generously chosen to give a rough idea of where solutions are to be found. In b) the nk -space has been reduced, and in c) a further reduction of the nk -space to an area where physically correct solutions are likely to be found, makes the intersections clearly visible. In c) the different intersections are marked by circles. Ideally, the three possible types of intersections (iso- R /iso- T , iso- Rb /iso- T and iso- R /iso- Rb) for a true solution, should coincide, but errors in the measured quantities (R , T and Rb), a wrongly determined film thickness and insufficient correctness of the optical model separate them.

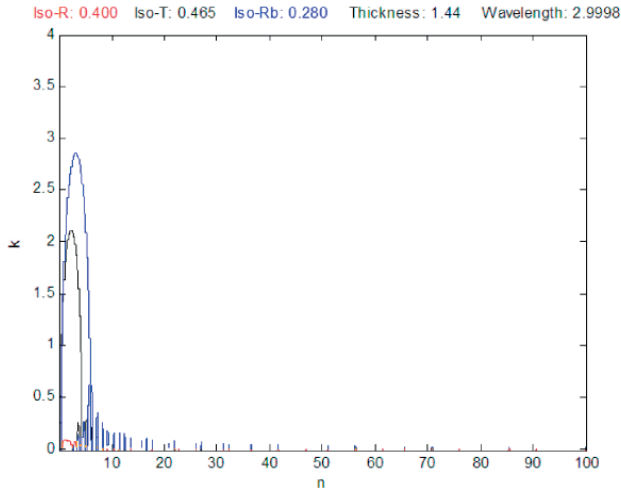


Figure 26: The iso-lines for R , T and Rb for the stack Cu(In,Ga)Se_2 /glass. The wavelength is $3 \mu\text{m}$ and the thickness of the Cu(In,Ga)Se_2 film is $1.44 \mu\text{m}$. Left: The nk -space is chosen very large to illustrate the spreading of the iso-lines.

In order to find physically correct solutions for n and k in the entire wavelength interval, all solutions found for a single wavelength as in Figure 26, were put together in $n(\lambda)$ and $k(\lambda)$ diagrams respectively. In Figure 27 such a diagram for $n(\lambda)$ is shown, but for simplicity only the intersections for the iso- R and iso- T is viewed. Since the physically correct solution must be continuous over the entire wavelength interval, this visualization offers a method to discern the true solution.

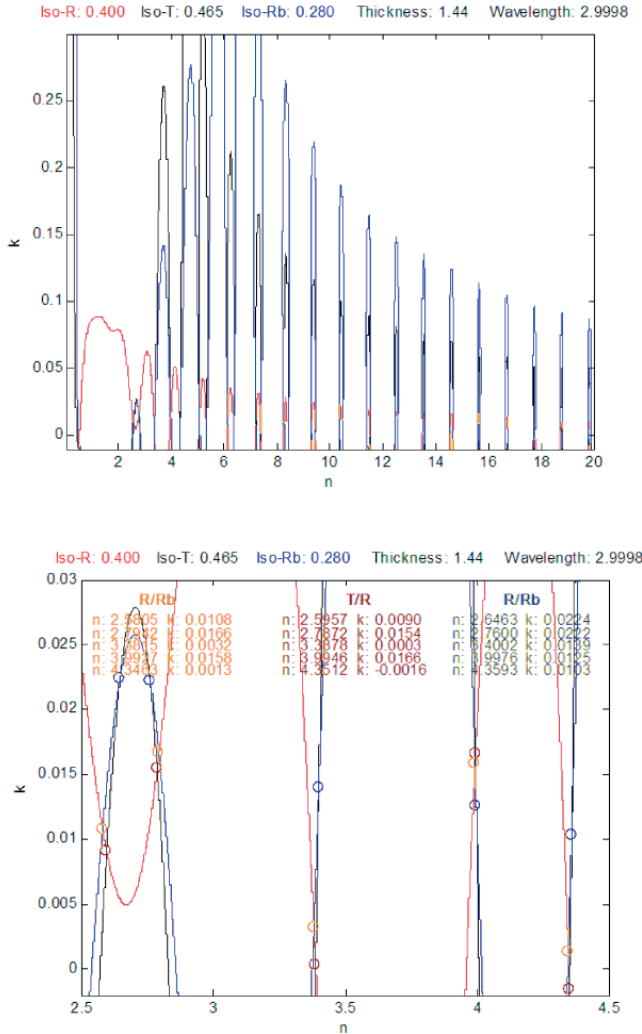


Figure 26: (continued)

Top: The nk -space has been reduced.

Bottom: A further reduction of the nk -space has been performed. The intersections of the iso-lines constitute the n and k solutions of Equations 27.

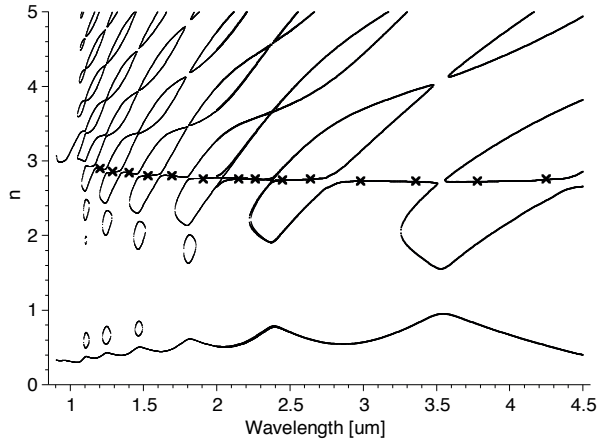


Figure 27: The resulting $n(\lambda)$ graph from intersections of iso-curves for the optical stack $\text{Cu(In,Ga)Se}_2/\text{glass}$ in the wavelength interval 1 μm to 4.5 μm . The physically correct solution is indicated by crosses.

The intersections of the iso-curves for the stack $\text{Cu}_x\text{Se}/\text{substrate}$ did not show the same multiplicity as for the stack $\text{Cu(In,Ga)Se}_2/\text{substrate}$. Only two intersections were found for most wavelengths. In Figure 28 the intersections are shown for the wavelength 3.0 μm , and a thickness for the Cu_xSe film of 20 nm.

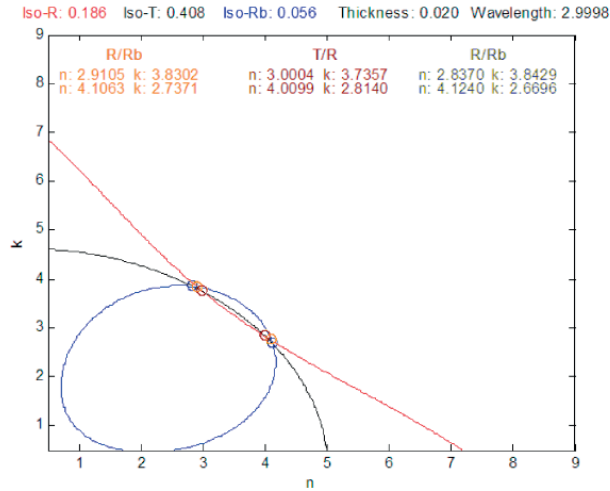


Figure 28: Intersections of the iso-curves generated of the stack optical $\text{Cu}_x\text{Se}/\text{glass}$ for the wavelength 3.0 μm . The picture is representative for the entire wavelength interval from 2 μm to 20 μm , but with values for n and k , increasing almost linearly with wavelength.

The resulting $n(\lambda)$ and $k(\lambda)$ graphs created by putting together all iso-curve intersections for every discrete wavelength, showed two sets of solutions,

$(n_1(\lambda), k_1(\lambda))$ and $(n_2(\lambda), k_2(\lambda))$. Since both sets of solutions were continuous, the method used to determine the physically correct solution used in the case of Cu(In,Ga)Se₂ could not be used. The solutions were such that $n_1(\lambda) \approx k_2(\lambda)$ and $n_2(\lambda) \approx k_1(\lambda)$. According to Equation 26b, the imaginary part of the complex dielectric function (ε_2) was then the same for both sets of solutions. For the real part (ε_1) in contrast, one solution became negative and decreasing with wavelength, whereas the other became positive and increasing. To conclude which of the solutions that was physically correct, Kramers-kronig (KK) analysis [43,44] was used. In Equation 30 it is shown how ε_1 relates to ε_2 according to KK-analysis. Even though Equation 30 states integration in the entire energy range, an extrapolation of ε_2 to lower and higher energies than the measured range, was sufficient to give clear indication of which solution of ε was physically correct.

$$\varepsilon_1(\omega) = 1 + \frac{2}{\pi} P \int_0^{\infty} \frac{\omega' \varepsilon_2(\omega')}{\omega'^2 - \omega^2} d\omega' \quad (30)$$

In section 4.3 the complex refractive indices (n and k) for Cu(In,Ga)Se₂ and Cu_xSe are used in a simulation. For this purpose, the n and k data were smoothed and extrapolated for the wavelength interval 2 μm to 20 μm as can be seen in Figure 32.

4.3 Results from the simulations

In paper IX simulation of the emissivity during the growth process was compared with measurements of the emissivity from a physical film. The procedure was as following:

A sample consisting of copper poor ($y \approx 0.9$) CIGS on a molybdenum coated soda lime glass was characterized optically by a spectrophotometer and compositionally with x-ray fluorescence (XRF). Then it was exposed for evaporation fluxes of copper and selenium in the deposition chamber for a short defined time. The measurements were repeated, followed by repeated depositions. The cycles of deposition followed by characterization were repeated until the copper concentration, y , reached about 1.3. This procedure corresponds to going in the reverse direction from the end of a CURO or a CUPRO process. In Figure 29 the gray shaded area shows the area of interest.

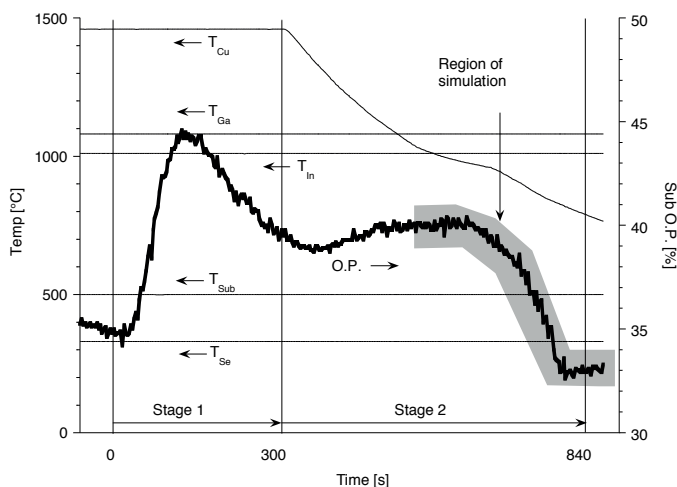


Figure 29: A copper poor sample fabricated by the CURO process, was exposed for repeated short fluxes of copper and selenium, after which it was analyzed regarding its compositional and optical properties. The gray shaded area indicates the area of investigation. From a compositional point of view, the CIGS film is following the CURO curve in the reverse direction compared to a normal deposition.

The co-evaporation of copper and selenium was performed in steps, each step with 10 s duration up to an accumulated deposition time of 120 s, then with 30 s duration up to 180 s followed by one deposition up to an accumulated time of 300 s.

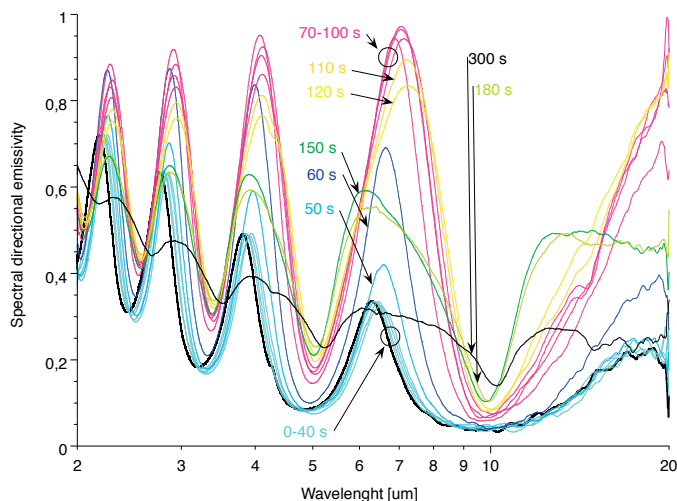


Figure 30: The spectral emissivity of a stack composed of various thickness of Cu_xSe on $\text{Cu}(\text{In,Ga})\text{Se}_2/\text{Mo}$. The spectral emissivity is calculated according to Equation 18. For the curves labeled 0-40 s no Cu_xSe has yet been formed on the stack. For 300 s the optical interference is weak due to opaqueness of the Cu_xSe layer. Further deposition would have led to bulk emissivity for Cu_xSe .

Compositional analysis was made with x-ray fluorescence (XRF) after each co-evaporation step. Analyses of reflectivity were also performed after each step using spectrophotometer in the wavelength interval from 2 μm up to 20 μm . From Equation 18 the emissivity was then calculated. The resulting spectral emissivity for various deposition times can be seen in Figure 30. From the spectral emissivity, the wavelength integrated emissivity is calculated according to Equation 31,

$$\varepsilon = \frac{\int_0^{\infty} \varepsilon(\lambda, T) M_{\lambda, b}(\lambda, T) d\lambda}{\int_0^{\infty} M_{\lambda, b}(\lambda, T) d\lambda} \quad (31)$$

where $M_{\lambda, b}(\lambda, T)$ is spectral irradiance for a black body given by Planck's radiation law Equation (12), and seen in Figure 12. The wavelength integrated emissivity for the sample for every step of the copper and selenium exposure is shown by circles in Figure 31.

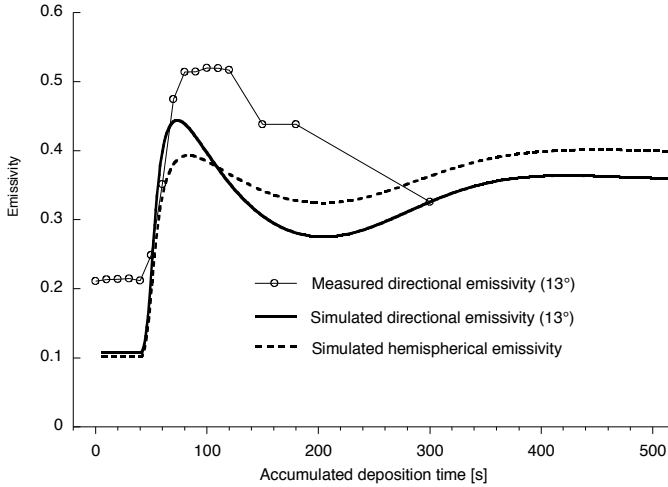


Figure 31: Wavelength integrated emissivity for an optical stack of $\text{Cu}_x\text{Se}/\text{Cu}(\text{In,Ga})\text{Se}_2/\text{Mo}$ at various thicknesses of Cu_xSe . During the first 40 seconds of exposure to copper and selenium, no Cu_xSe is formed and consequently the emissivity is constant and at a low level. The difference in the level for the simulated and the measured emissivity during the first 40 seconds may be explained by macroscopic differences between the two films such as e.g. surface roughness. This difference in emissivity level continues after Cu_xSe formation, but the relative change is similar.

The simulation of the emissivity of the above sample is described as follows: The optical model described in chapter 3.1 was used to calculate the reflectivity of the optical stack $\text{Cu}_x\text{Se}/\text{Cu}(\text{In,Ga})\text{Se}_2/\text{Mo}$. Equation 19 was then

used to calculate the emissivity. Since the optical model needs the complex refractive indices for all layers involved in the stack these must be provided in the simulation. For molybdenum, data of n and k from *Ordal et al* were used [45]. For Cu(In,Ga)Se_2 and Cu_xSe data had to be derived as described in section 4.2. The derived n and k data for Cu(In,Ga)Se_2 were not continuous over the entire wavelength interval needed ($2\text{ }\mu\text{m}$ to $20\text{ }\mu\text{m}$), why extrapolation of the data was necessary. The smoothed curves for Cu_xSe and Cu(In,Ga)Se_2 that were used in the simulation are shown in Figure 32.

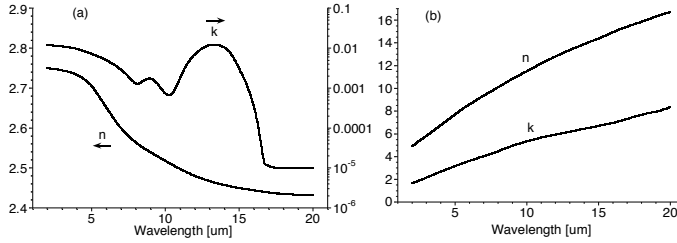


Figure 32: Extrapolated and smoothed optical constants (n and k) of a) Cu(In,Ga)Se_2 and b) Cu_xSe . The data for n and k were used in a simulation of the emissivity of a growing CIGS film in paper IX. The determination of the optical constants was performed by use of an optical model and reflectivity and transmissivity measurements described in detail in paper VIII.

The thickness of the molybdenum layer used in the simulation was set to 400 nm but is almost uncritical since a thickness above a few nanometers will be enough for opaqueness. For the thicknesses of Cu(In,Ga)Se_2 and Cu_xSe during the simulation the following strategy was used: For deposition of copper and selenium on to a copper deficient Cu(In,Ga)Se_2 film, the thickness will not increase since the size of the unit cell is assumed not to change significantly when copper atoms fill copper vacancies in the lattice. The thickness of Cu_xSe is zero as long as the Cu(In,Ga)Se_2 is copper deficient, and increases thereafter linearly. The rate of increase for the Cu_xSe film thickness was calculated using the x-ray fluorescence (XRF) data. The simulation of the emissivity is shown as the solid line in Figure 31. Qualitatively, the agreement between the measured and the simulated emissivity is good. The peak behavior (maximum emissivity) is clearly seen for both.

To be able to correlate the emissivity from the optical simulation with the monitored OP-signal monitored during film deposition, the simulation had to be modified. Since the OP-signal is due to power loss by radiation, this radiation must be simulated. The radiation from the substrate is hemispherically spread, therefore the simulation was modified to also be hemispherically spread. In Figure 33 it is shown how the directional emissivity as a function of angle is changed when the layer of Cu_xSe is increased.

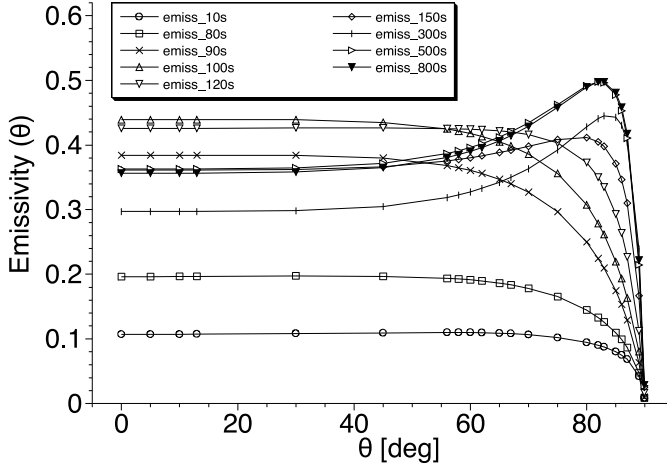


Figure 33: Wavelength integrated directional emissivity as function of directional angle for an optical stack of $\text{Cu}_x\text{Se}/\text{Cu}(\text{In,Ga})\text{Se}_2/\text{Mo}$, for various thickness of Cu_xSe . The increase in the emissivity for high angles is a typical behavior for conducting materials.

When the Cu_xSe layer has grown sufficiently thick, the directional emissivity of the stack is governed by the bulk property of Cu_xSe . The tendency of increased directional emissivity for high angles is typical behavior of metals and metal-like materials [46]. A practical consequence of the angular difference of the emissivity for copper rich and copper poor CIGS could be if optical measurements of the CIGS growth is done in a narrow solid angle interval at high angles.

The angular integration of the angular dependent emissivity yields the hemispherical emissivity as in Equation 32 [47].

$$\varepsilon_h = 2 \int_0^{\pi/2} \varepsilon_d(\theta) \sin(\theta) \cos(\theta) d\theta \quad (32)$$

The resulting hemispherical emissivity as a function of accumulated deposited copper and selenium is seen in Figure 31. As can be seen in Figure 31, the hemispherical emissivity is more attenuated compared to the directional emissivity at an angle of 13°. Nevertheless, the peak behavior is still evident after the angular integration. This means that the OP-signal during growth should perform a positive peak when the Cu_xSe layer is decreasing in a CURO or CUPRO process. If such a peak is not detected, the reason may be found within the equipment or in a lack of thermal steady state as was discussed in section 3.9.

5. Conclusion and outlook

In this thesis I have described methods for fabrication of Cu(In,Ga)Se_2 absorber layers for solar cells. The deposition process of the CIGS films has been performed with physical vapor deposition from elemental sources for copper, indium, gallium and selenium. Three processes for deposition of CIGS has been studied in detail in this thesis, CURO (copper rich, then copper source off), INRO (indium rich, then indium source off) and CUPRO (copper poor, then rich, then copper source off). A description was given of how the fabricated films can be monitored during fabrication using their radiative behavior. Also the differences in grain size obtained from different processes have been studied. The processes CURO and CUPRO exhibit larger grains than the INRO process due to the presence of Cu_xSe during part of the deposition. It has been found that the emissivity of the CIGS film, which governs the thermal radiation, is due to the relation between the segregated Cu_xSe phase and the Cu(In,Ga)Se_2 film on the molybdenum coated glass substrate. The CUPRO process has shown excellent behavior in terms of possibility to be controlled and monitored by the use of end-point detection. It gives a smooth surface and has produced solar cell material which gives devices with above 15 % efficiency. For all above mentioned processes (CURO, INRO and CUPRO), a constant temperature (500 °C) of the substrate has been used. In the transition between copper rich and copper poor CIGS or vice versa, the emissivity and thereby also the electrical power to the substrate heater becomes the control parameter for the composition of the film.

In the thesis the optical constants of both Cu_xSe and Cu(In,Ga)Se_2 have been derived for the wavelength interval from 1 μm to 20 μm . This was done in order to be able to simulate the emissivity for a growing CIGS film. Both the simulation and the determination of the optical constants used an optical model that assumes specular transfer of radiation from layer to layer. In reality scattering interfaces may be created between smooth layers. It would be preferable to use optical models dealing with diffuse light scattering for refined accuracy of the optical constants, and better quantitative agreement between simulation and measurement of the emissivity for growing CIGS.

Finally a conclusive remark about the measuring of emissivity indirectly by monitoring the infrared radiation by means of the electric power to the substrate heater. It is probably a better idea to measure the emissivity directly at a wavelength interval decoupled from the wavelength interval related to

the temperature for the substrate. In such cases, thermal dynamic artifacts caused by thermal loads within the substrate heater and other parts of the deposition system are prevented from giving contributions to the readout signal.

7. Summary in Swedish

7.1 Solenergi

Solens strålar som träffar jorden under en dag innehåller flera tiopotenser mer energi än vad vi människor använder i form av elektricitet. Potentialen för att samla upp en bråkdel av denna energi i form av ljus och omvandla den till elektrisk energi med hjälp av solceller är enorm. Solcellsmoduler finns redan idag kommersiellt tillgängliga på marknaden. Forskningen som utförs på solceller syftar i huvudsak till att dels göra solcellerna bättre, dels finna metoder och tillverkningsätt som gör solcellsmodulerna billigare. Denna avhandling har främst behandlat det tidigare området.

7.2 Solcellen

En solcell i sin enklaste form, se bild 1, består av ett halvledarmaterial, dopat på så sätt att en sida har ett överskott på negativt laddade joner medan en annan sida har ett överskott på positivt laddade joner och överskott på elektroner. I ett område nära övergången mellan de olika dopningarna kommer överskott av elektroner att diffundera över till sidan med underskott av elektroner. Kvar blir endast de positiva och negativa jonerna. På grund härav uppstår ett elektriskt fält i detta område. När ljus av rätt våglängd (energi) träffar atomer som befinner sig här eller i snar närhet, exciteras (frigörs) elektroner från atomerna. Det bildas dels en fri elektron, dels ”frånvaron av en elektron”, ett så kallat hål. Dessa separeras till var sin sida om det elektriska fältet, varpå en elektrisk spänning uppstår mellan de båda olika dopade sidorna. Genom att ansluta elektriska kontakter kan en ström fås att flyta i en extern krets. Detta är själva drivkraften till en solcells funktion.

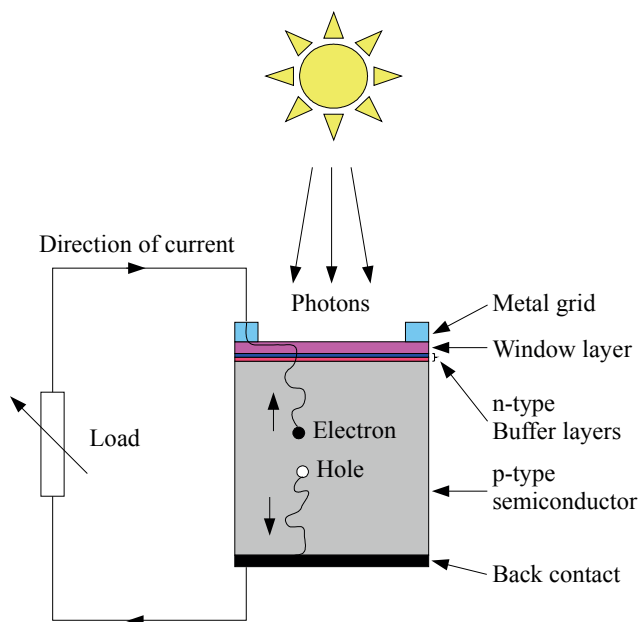


Bild 1: När ljuskvanta, fotoner, träffar solcellen, passerar de först fönsterlagret och buffertlagren för att sedan komma in i absorbatoren. I absorbatoren exciterar fotonerna atomer som släpper ifrån sig en elektron. Det som blir kvar efter att elektronen lämnat atomen kallas i detta sammanhang för ett hål, och betar sig som en positiv laddning. De skapade elektron-hål-paren kommer att separeras av ett elektriskt fält som finns inbyggt i solcellen. Ju fler fotoner som absorberas ju starkare ström kan solcellen skapa.

7.3 CIGS-solceller

En tunnfilmssolcell består vanligen av ett flertal olika lager, vart och ett med sin specifika uppgift, se bild 2. Den delen av solcellen där ljuset absorberas varpå par av elektroner och hål skapas kallas absorbatoren. Denna avhandling beskriver hur tillverkning av absorbatoren av halvledarmaterialet $\text{Cu}(\text{In,Ga})\text{Se}_2$ (CIGS) kan göras och hur tillverkningsprocessen kan övervakas. Först ges här en mycket kort sammanfattning av solcellens övriga lager: Då de elektriskt aktiva lagren är mycket tunna (i storleksordningen μm) så används ett substrat av fönsterglas som fysisk bärare av de olika skikten. På substratet beläggs ett tunt ($0.5 \mu\text{m}$) lager av metallen molybden som fungerar som bakkontakt för solcellen. Därefter följer tillverkningen av absorbatoren som beskrivs utförligare längre fram. På absorbatoren appliceras ytterligare minst tre skikt, som har till uppgift dels att utgöra en motdopad partner till absorbatorskiktet, dels utgöra den elektriskt ledande men också för ljus transparenta framkontakten. Tillverkningen av absorbatoren görs i en vakuumkammare med en metod kallad samförångning, där de till

absorbatorn ingående grundämnena förångas simultant med en förångningskälla per grundämne. Ångorna från metallerna koppar, indium och gallium samt från halvledaren selen får kondensera på substratet som med hjälp av en substratvärmare hålls vid 500 °C. Substratvärmaren värmer substratet med hjälp av halogenlampor. För temperaturkontroll avläses temperaturen på substratets ovansida med ett termoelement. Termoelementet skickar information till en regulator som kan öka eller minska den elektriska effekten, (*Output Power*-signalen) till substratvärmaren så att temperaturen på substratet kan hållas konstant. Från substratets undersida, det vill säga där absorbatorn skall tillväxa, läcker det bort effekt i form av värmestrålning. Denna effekt beror av ytans emissivitet.

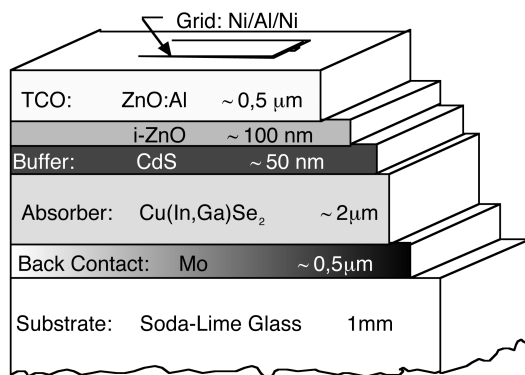


Bild 2: De olika lagren av material för en CIGS-solcell. Glaset används för fysisk support av den tunna solcellen. Filmen högst upp utgör den så kallade framkontakten som är elektriskt ledande samt transparent för solljuset. I absorbatorskiktet omvandlas solljuset till elektrisk energi via laddningsseparering. De två skikten mellan absorbatorskiktet och framkontakten är så kallade buffertskikt.

7.4 Sammansättningskontroll och CIGS-processer

För att solcellen skall fungera måste kvoten mellan antalet kopparatomer och indium- och galliumatomer ($y = \text{Cu}/(\text{In}+\text{Ga})$) i den färdigtillverkade absorbatorn vara under ett. Är y större än ett bildas förutom det önskade lagret av Cu(In,Ga)Se₂ också en segregerad fas av Cu_xSe. Under tillverkningsprocessen kan dock y tillåtas överstiga ett. Den bildade Cu_xSe kommer då att till stor del lägga sig som ett halvflytande lager ovanpå Cu(In,Ga)Se₂ lagret. I avhandlingen visas hur emissivitet hos den tillväxande CIGS filmen ändras, och kan läsas av genom OP-signalen, beroende på om Cu_xSe finns ovanpå Cu(In,Ga)Se₂ filmen eller inte.

För tillverkningen av Cu(In,Ga)Se_2 absorbatoren har olika deponeringsstrategier, recept, använts. Det mest använda är två-stegs receptet CURO, där i det första steget förångningskällorna är inställda så, att CIGS filmen blir kopparrik. Här bildas följaktligen Cu(In,Ga)Se_2 med ett lager Cu_xSe ovanpå. I bild 3 visas hur OP-signalen varierar genom de olika faserna i en CURO process. Emissiviteten för denna konstellation blir hög, varför detta kan avläsas som en hög OP-signal. I andra steget stängs förångningskällan för koppar av, varefter kopparången snabbt försvinner. För det växande Cu(In,Ga)Se_2 lagret blir det emellertid till en början ingen skillnad då de erforderliga kopparatomerna tas från det halvflytande Cu_xSe lagret, som nu krymper. När Cu_xSe lagret är helt borta har emissiviteten antagit en lägre nivå som också den utläses genom OP-signalen. Det andra steget fortsätter ytterligare en tid sedan all Cu_xSe försvunnit, varefter Cu(In,Ga)Se_2 lagret blir så kallat kopparfattigt, och lämpligt att använda som absorbatör, och processen avbryts. Karakteristiskt för CIGS tillverkat med CURO receptet är att de polykristallina kornen som utgör Cu(In,Ga)Se_2 lagret, blir relativt stora. Det anses bero på närvaron av Cu_xSe under tillväxten. Ett eventuellt problem med CURO är att det förekommer skrevor i det färdiga Cu(In,Ga)Se_2 lagret. Tesen för dessas uppkomst är att Cu_xSe befinner sig delvis mellan kornen av Cu(In,Ga)Se_2 i första steget, och att när denna förbrukas under andra steget uppstår hålrum. Det har funnits vara en korrelation mellan djupet på dessa skrevor och kvoten mellan längden på första steget till längden på andra steget. Vid analys med röntgendiffraktion, (XRD) har Cu(In,Ga)Se_2 filmer tillverkade med CURO-receptet haft en tydlig önskad (112) kristallorientering.

Ett annat använt deponeringsrecept är CUPRO, som består av tre steg. Det första där kopparfattig CIGS är växt med med konstanta flöden från alla förångningskällor. OP-signalen är här låg, eftersom emissiviteten är låg. I andra steget ökas flödet av ånga från förångningskällan för koppar. Följden blir att kopparvakanser i Cu(In,Ga)Se_2 gittret först fylls upp. Därefter startar segregering av Cu_xSe som bildar ett separat skikt på ytan av Cu(In,Ga)Se_2 -filmen. Detta ger en förhöjd emissivitet, varpå OP-signalen ökar. Tredje steget är identiskt med det andra i CURO processen. Vid analys av CIGS tillverkad med CUPRO processen har visats att det första steget ger CIGS med relativt små korn, men utan skrevor. Under andra steget sker en ombildning av kornen så att dessa ökar i storlek, vilken bibehålls genom tredje steget. Till skillnad från CURO processen visar resultat från XRD att den önskade kristallorienteringen för CUPRO filmer är (220)(204). Denna orientering initieras under den kopparfattiga tillväxten i första steget, och bibehålls processen igenom. Både CURO och CUPRO har varierats ifråga om processernas längd. Resultatet har dels varit Cu(In,Ga)Se_2 av god solcellskvalitet, dels insikten att emissiviteten för filmen hela tiden befunnit sig i jämvikt med filmtillväxten. Detta är viktigt efter som det öppnar för

möjligheten till snabbare deponering, med bibehållen rapportering av CIGS materialets tillväxtstatus genom dess värmestrålningsegenskaper.

Dock är det ett faktum att OP-signalen påverkas inte bara av den växande CIGS filmens strålningsegenskaper, utan också av dynamiken hos förångningsutrustningen, genom att termisk energi upplagras i till exempel substratvärmare och kammurväggar, eller av att förångningskällor stängs av eller sätts på.

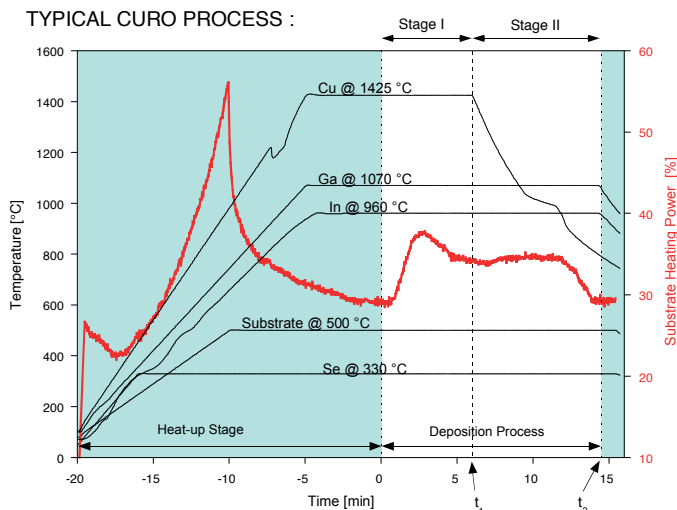


Bild 3: Temperaturer för förångningskällor och substratvärmare samt OP-signal för en CURO-process.

7.5 IR-emissivitet hos CIGS-skikt

För att undersöka hur strålningsegenskaperna hos CIGS filmen under tillverkning påverkas av y -värdet, alltså graden av kopparrikhet, har simulering av emissiviteten genomförts. Genom simulering kan filmens emissivitet frikopplas från yttre påverkan från förångningsutrustningen. Simuleringen bygger på att en optisk modell, snarlik den verkliga, beräknar emissiviteten. Modellen använder en matrismetod där emissiviteten beräknas för varje diskret våglängd för sig. De skikt som ingår i den optiska modellen skall ha kända tjocklekar, samt kända optiska konstanter, till exempel det komplexa brytningsindexet $N = n + ik$. Modellen är begränsad till att endast kunna hantera spekulär spridning, vilket är en förenkling då det i verkligheten även förekommer diffus spridning av ljus i vissa gränsskikt. Det våglängdsintervall som är intressant i detta fall är från $2\ \mu\text{m}$ till $20\ \mu\text{m}$, då det är mellan dessa våglängder värmestrålning vid $500\ ^\circ\text{C}$ förekommer. Den optiska stacken som används vid simuleringen är $\text{Cu}_x\text{Se}/\text{Cu}(\text{In,Ga})\text{Se}_2/\text{Mo}$.

Optiska konstanterna ($n(\lambda)$ och $k(\lambda)$) för Cu_xSe och $\text{Cu}(\text{In,Ga})\text{Se}_2$ var inte kända för det önskade våglängdsintervallet, varför det var nödvändigt att först bestämma dessa innan simuleringen kunde utföras.

Metoden som användes vid bestämningen av de optiska konstanterna var reflektans- och transmittansmätningar (R och T), i kombination med den ovan beskrivna optiska modellen, men nu med en optisk stack bestående av film/substrat, där film antingen var Cu_xSe eller $\text{Cu}(\text{In,Ga})\text{Se}_2$ och substrat antingen var glas eller dubbelpolerat högresistivt kisel. Se bild 4. Kärnan i problemet blir att lösa ekvationssystemet $R_{\text{uppmätt}} - R_{\text{beräknat}} = 0$, $T_{\text{uppmätt}} - T_{\text{beräknat}} = 0$ för den optiska stacken. För att reducera antalet obestämda parametrar beräknas optiska konstanter först för en stack bestående av endast substrat. Sedan byggs stacken upp till att innehålla film och substrat, varpå de optiska konstanterna för filmen beräknas. De optiska konstanterna (n och k) söks i ett tillräckligt stort område (intervall av n respektive k), så att de säkert finns inom detta. Området diskretiseras sedan varpå varje diskret par av (n_i, k_j) testas för ekvationssystemet. Ett välkänt problem med denna metod är att det oftast finns multipla lösningar (n och k) som satisfierar ekvationssystemet. Det finns emellertid endast ett par (n och k) som motsvarar den sanna fysikaliska lösningen för varje våglängd. Därför utarbetades en metod där alla lösningar för alla våglängder åskådliggjordes simultant, och de sanna lösningarna kunde identifieras med hjälp av kontinuitetskriteriet att lösningarna för $n(\lambda)$ och $k(\lambda)$ måste vara kontinuerliga genom hela våglängdsintervallet. Lösningar bestämdes för Cu_xSe inom hela intervallet, medan det för $\text{Cu}(\text{In,Ga})\text{Se}_2$ uppstod luckor i intervallet där lösningar inte kunde hittas. För simuleringen av den växande CIGS filmen extrapolerades data i dessa luckor så att ett kontinuerligt intervall för n och k fanns tillgängligt.

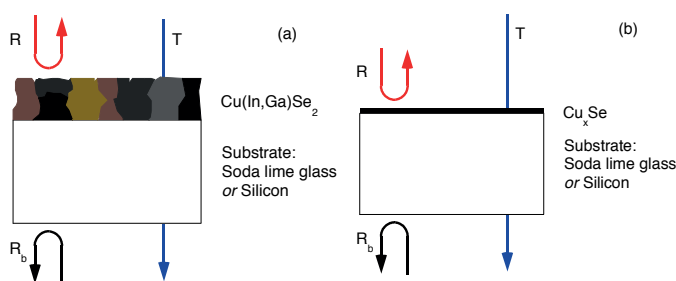


Bild 4: För att bestämma de optiska konstanterna n och k , mäts reflektans och transmittans på optiska stackar bestående av film och substrat. Substratens n och k , har dessförinnan bestämts genom mätningar på endast substraten.

Simuleringen av emissiviteten visade tydliga likheter med vad som tidigare kunnat observeras med hjälp av OP-signalen. Bland annat sågs att det förekommer ett maximum i emissivitet hos CIGS filmen då en viss tjocklek

av Cu_xSe ligger på $\text{Cu}(\text{In,Ga})\text{Se}_2$. Detta fenomen har observerats som ett lokalt maximum för OP-signalen i CURO processen i andra steget då tjockleken på Cu_xSe lagret krymper, innan CIGS filmen blir kopparfattig. Den teoretiska kunskapen om detta fenomen kan användas till förbättrad processtyrning i industriell tillverkning av CIGS solceller.

Bibliography

- [1] *World Energy Outlook 2008*, International Energy Agency (2008)
- [2] European Photovoltaics Industry Association, Global market outlook for photovoltaics until 2015 (May 2011)
- [3] I. Repins, M. A. Contreras, B. Egaas, C. DeHart, J. Scharf, C. L. Perkins, B. To and R. Nufi, "19.9%-efficient ZnO/CdS/CuInGaSe₂ Solar Cell with 81.2% Fill Factor", *Progress in Photovoltaics: Research and Applications*, **16** (2008), pp. 235-239
- [4] IEC-904-3, *IEC Standard* i.e. 1000 W/m² AM1.5 normal to cell surface at 25 °C, 1989.
- [5] H-W. Schock, "CuInSe₂ and Other Chalcopyrite-Based Solar Cells", *MRS Bulletin* **10** (1993), no. 10, p. 43-44
- [6] S. Zhang, S. -H. Wei, A. Zunger, "Stabilization of Ternary Compounds via Ordered Arrays of Defect Pairs" *Phys. Rev. Lett.* **78**, 4059–4062 (1997)
- [7] J. R. Tuttle, A. Szalaj and J. Keane, "A 15.2% AM0 / 1433 W/KG THIN-FILM CU(IN,GA)SE₂ SOLAR CELL FOR SPACE APPLICATIONS", in: *Proceedings 28th IEEE Photovoltaic Specialist Conference*, Anchorage (2000) p. 1043-1045
- [8] K. Otte, L. Makhova, A. Braun and I. Kononov, "Flexible Cu(In,Ga)Se₂ thin-film solar cells for space applications", *Thin Solid Films*, **511-512** (2006), p. 613-622
- [9] S. H. Wei and A. Zunger, "Band offsets and optical bowings of chalcopyrites and Zn-based II-IV alloys", *Journal of Applied Physics*, **78** (1995) p. 3846-3856
- [10] J. Kessler, M. Bodegård, J. Hedström and L. Stolt, "Baseline Cu(In,Ga)Se₂ device production: Control and statistical significance", *Solar Energy Materials & Solar Cells*, **67** (2001), p. 67-76
- [11] D. Braunger, D. Hariskos, G. Bilger, U. Rau, H. W. Schock, "Influence of sodium on the growth of polycrystalline Cu(In,Ga)Se₂ thin films", *Thin Solid Films*, **361-362** (2000), p. 161-166
- [12] A. Romeo, M. Terheggen, D. Abou-Ras, D. L. Bätzner, F. -J. Haug, M. Kälin, D. Rudmann and A. N. Tiwari, "Development of Thin-film Cu(In,Ga)Se₂ and

- CdTe Solar cells”, *Progress in Photovoltaics: Research and Applications* **12** (2004), p.93-111
- [13] J. Malmström, O Lundberg, and L. Stolt, “Potential for light trapping in Cu(In,Ga)Se₂ solar cells”, in: *Proceedings 3rd World conference on Photovoltaic Energy Conversion* (WCPEC-3 Organizing Committee, Osaka, 2003), **1** p. 344-347
- [14] J. Malmström, S Schleußner, and L. Stolt, “Enhanced back reflectance and quantum efficiency in Cu(In,Ga)Se₂ thin film solar cells with a ZrN back reflector”, *Applied Physics Letters* **85** (2004) p. 2634-2636
- [15] B. Canava, J. F. Guillemoles, J. Vigneron, D. Lincot and A. Etcheberry, “Chemical elaboration of well defined Cu(In,Ga)Se₂ surfaces after aqueous oxidation etching”, *Journal of Physics and Chemistry of Solids*, **64** (1996), p. 1791-1796
- [16] A. J. Nelson, A. M. Gabor, M. A. Contreras, A. Mason, P. Asoka-Kumar and K. G. Lynn, “Relation of polycrystalline Cu(In,Ga)Se₂ device efficiency with junction depth and interfacial structure”, *Solar Energy Materials and Solar Cells*, **41-43** (1996), p. 315-323
- [17] T. Törndahl, A. Hultqvist, C. Platzer-Björkman, M. Edoff, E. Coronel and K. Leifer, “The Effect of Zn_{1-x}Mg_xO Buffer Layer Deposition Temperature on Cu(In,Ga)Se₂ Solar Cells: A Study of the Buffer/absorber Interface”, *Progress in Photovoltaics: Research and Applications* **17** (2009), p.115-125
- [18] Ullmann's Chemical Engineering and Plant Design, Volumes 1-2, s.556
- [19] King-Ning Tu, James W. Mayer, and Leonard C. Feldman, in: *Electronic Thin Film Science for Electrical Engineers and Materials Scientists*, Macmillan, New York, 1992, p. 101-102.
- [20] M. Ruckh, D. Schmid, M. Kaiser, R. Schäffler, T. Walter and H. W. Schock, “Influence of Substrates on the Electrical Properties of Cu(In,Ga)Se₂ Thin Films”, in *Proc. 1st World Conference on Photovoltaic Energy Conversion*, edited by: (IEEE, New York, , 1994), 156 (1994)
- [21] R. Klenk, T. Walter, H.-W. Schock and D. Cahen, “PHYSICAL VAPOR DEPOSITION OF CuInX₂ (X=s, Se) THIN FILMS: A VAPOR MODEL FOR THE GROWTH MECHANISM”, *Solid State Phenomena*, **37-38** (1994) p. 509-514
- [22] S. Nishiwaki, N. Kohara, T. Negami, H. Miyake and T. Wada, “Microstructure of Cu(In,Ga)Se₂ Films Deposited in Low Se Vapor pressure”, *Japanese Journal of Applied Physics*, **38** (1999), p. 2888-2892
- [23] D. Schmid, M. Ruckh and H. W. Schock, “Photoemission studies Cu(In,Ga)Se₂ thin films and related binary selenides”, *Applied Surface Science*, **103** (1996), p. 409-439

- [24] R. Klenk, T. Walter, H.-W. Schock and D. Cahen, "A Model for the Successful Growth of Poly-crystalline Films of CuInSe₂ by Multisource Physical Vacuum Evaporation", *Advanced Materials*, **5** (1993) p. 114-119
- [25] M. Nishitani, T. Negami, T. Wada, "Composition monitoring method in CuInSe₂ thin film preparation", *Thin Solid Films* **258** (1995) p. 313
- [26] N. Kohara, T. Negami, M. Nishitani, T. Wada, "Preparation of Device-Quality Cu(In, Ga)Se₂ Thin Films Deposited by Coevaporation with Composition Monitor", *Jpn. J. Appl. Phys.*, Vol. 34, No 9A (1995) p. 1141
- [27] T. Negami, M. Nishitani, N. Kohara, Y. Hashimoto, T. Wada, *Material Research Society Symposium, Proc.* **436** (1996) p. 267
- [28] O. Lundberg, J. Lu, A. Rockett, M. Edoff and L. Stolt, "Diffusion of indium and gallium in Cu(In,Ga)Se₂ thin film solar cells", *Journal of Physics and Chemistry of Solids*, **64** (2003) pp. 1499-1504
- [29] M. Marudachalam, R. W. Birkmire, H. Hichri, J. M. Schultz, A. Swartzlander and M. M. Al-Jassim, "Phases, morphology, and diffusion in CuIn_xGa_{1-x}Se₂ thin films", *Journal of Applied Physics*, **82** (1997), pp. 2896-2905
- [30] W.S. Chen, and R.A. Mickelsen, *SPIE Proceedings* 248 (1980) p. 62
- [31] R. A. Mickelsen and W. S. Chen, in *Proceeding of 15th IEEE Photovoltaic Conference*, San Diego (1981), p. 800-804
- [32] V. Alberts and M. L. Chenene, "In-depth compositional uniformity of CuInSe₂ prepared by two-stage growth sequences", *Journal of Physics D: Applied Physics* **32** (1999) p. 3093-3098
- [33] S. Kuranouchi and A. Yoshida, "Annealing effects of CuInSe₂ films prepared by pulsed laser deposition", *Thin Solid Films*, **343-344** (1999) p. 123-126
- [34] D. Liao and A. Rockett, "(220)-Oriented – Evidence that it may improve Solar Cell performance", in: *Proceedings 28th IEEE Photovoltaic Specialist Conference*, Anchorage (2000) p. 446-449
- [35] W. N. Shafarman and J. Zhu, "Effect of substrate temperature and deposition profile on evaporated Cu(In,Ga)Se₂ film and devices", *Thin Solid Films*, **361-362** (2000), p. 473-477
- [36] J. Barela and K. Chrzanowski, "Pyrometer for temperature measurement of selective objects of unknown and variable emissivity" in: *Quantitative InfraRed Thermography*, Reims, 2000-048
- [37] P. Pfrommer, K. J. Lomas, C. Seale, and Chr. Kupke, "The radiation transfer through coated and tinted glazing", *Solar Energy*, **54**, No 5, p. 287-299
- [38] Guozhong Cao, *Nanostructures and Nanomaterials*, Imperial College Press, London, 2004.

- [39] K. Orgassa, U. Rau, H. -W. Schock and J. H. Werner, "Optical Constants of Cu(In,Ga)Se₂ Thin Films From Normal Incidence Transmittance and Reflectance", in proceedings 3rd World Conference on Photovoltaic Energy Conversion, K. Kurokawa, L. L. Kazmerski, B. McNelis, M. Yamaguchi, C. Wronski, and W. C. Sinke, Eds. Osaka, Japan: WCPEC-3 Organizing Committee, 2003, pp. 2P-A8-04
- [40] P. -O. Nilsson, "Determination of Optical Constants from Intensity Measurements at Normal Incidence", *Applied Optics*, **7** (1968), p. 435-443
- [41] J. E. Nestell, jr. and R. W. Christy, "Derivation of Optical Constants of Metals from Thin-Film Measurements at Oblique Incident", *Applied Optics*, **11** (1972), p. 643-651
- [42] A. B. Djurišić, T. Fritz and K. Leo, "Determination of optical constants of thin absorbing films from normal incidence reflectance and transmittance measurements", *Optics Communications*, **166** (1999), p. 35-43
- [43] C. F. Klingshirn "Semiconductor Optics", Berlin: Springer, 1997
- [44] A. Hultåker, "Transparent Conductive Tin Doped Indium Oxide", Ph.D. Thesis, Acta Universitatis Upsaliensis, Uppsala University, Sweden, 2002.
- [45] M. A. Ordal, R. L. Bell, R. W. Alexander, Jr., L. A. Newquist and M. R. Querry, "Optical properties of Al, Fe, Ti, Ta, W and Mo at submillimeter wavelengths", *Applied Optics* **27** (1988), Issue 6, p. 1203-1209
- [46] N. Menn, Practical Optics (Elsevier Academic Press, New York, 2004)
- [47] M. Rubin, "OPTICAL PROPERTIES OF SODA LIME SILICA GLASSES", *Solar Energy Materials* **12** (1985), p 275-288

Acta Universitatis Upsaliensis

*Digital Comprehensive Summaries of Uppsala Dissertations
from the Faculty of Science and Technology 909*

Editor: The Dean of the Faculty of Science and Technology

A doctoral dissertation from the Faculty of Science and Technology, Uppsala University, is usually a summary of a number of papers. A few copies of the complete dissertation are kept at major Swedish research libraries, while the summary alone is distributed internationally through the series Digital Comprehensive Summaries of Uppsala Dissertations from the Faculty of Science and Technology.



ACTA
UNIVERSITATIS
UPSALIENSIS
UPPSALA
2012

Distribution: publications.uu.se
urn:nbn:se:uu:diva-170437